ATLAS CONF Note

ATLAS-CONF-2023-045

August 19, 2023

Search for a new leptonically decaying neutral vector boson in association with missing transverse energy in proton–proton collisions at $\sqrt{s} = 13$ TeV with the ATLAS detector

The ATLAS Collaboration

A search for dark matter particles produced in association with a new neutral vector boson is performed using proton–proton collisions at $\sqrt{s} = 13$ TeV, corresponding to an integrated luminosity of 140 fb^{-1} recorded by the ATLAS detector at the Large Hadron Collider. Decays of the Z' boson to same-flavour light leptons ($e^+e^-/\mu^+\mu^-$) are studied for Z' masses above 200 GeV. No significant excess over the Standard Model prediction is observed. The results of this search are interpreted for several dark-Higgs and light-vector benchmark model scenarios. Cross-section limits are set considering each benchmark scenario, as well as limits on the coupling of the Z' to leptons.

1 Introduction

Numerous cosmological observations indicate that a large part of the mass of the universe is composed of dark matter (DM), yet its exact, possibly particle, nature and its connection to the Standard model (SM) of particle physics remain unknown. The discovery of DM particles and its interactions with SM particles is one of the greatest quests in particle physics and cosmology today. Several different experimental approaches are being exploited. Indirect detection experiments search for signs of DM annihilation or decays in outer space, while direct detection experiments are sensitive to low-energy recoils of nuclei induced by interactions with DM particles from the galactic halo. The interpretation of these searches is subject to astrophysical uncertainties in DM abundance and composition. Searches at particle colliders, for which these uncertainties are irrelevant, are complementary if DM candidates can be produced in particle collisions. Weakly interacting massive particles (WIMPs), one of the most commonly considered candidates for DM, could be produced in proton–proton (pp) collisions at the Large Hadron Collider (LHC) and detected by measuring the momentum imbalance, missing transverse energy ($E_{\mathrm{T}}^{\mathrm{miss}}$), associated with the recoiling SM particles.

This analysis focuses on DM production in association with a new neutral vector boson Z' [1] decaying to a pair of same-flavour light leptons ($e^+e^-/\mu^+\mu^-$). It extends the existing inclusive resonant searches in the dilepton final state at LHC [2, 3] by adding a requirement on the missing transverse energy. This search is complementary to the results presented in Ref. [4], which explored the hadronic decays of the Z' boson assuming no coupling to leptons, and improves upon those presented in Ref. [5], which explored the dimuon decay of the Z' boson using 11.6 fb^{-1}of CMS open-data at a centre-of-mass energy of $\sqrt{s} = 8$ TeV.

This analysis considers two example benchmark models [1]: the dark-Higgs model, shown in Figure 1(a), and the light-vector model, shown in Figure 1(b). In the dark-Higgs model, a dark-sector Higgs boson h_{D} can be radiated from the Z' boson and decay to a pair of dark matter particles ($\chi\chi$). In the light-vector case, the Z' boson has an off-diagonal coupling to the χ_1 and χ_2 dark-sector particles and thus the heavier state χ_2 decays to a lighter dark matter candidate χ_1 and a Z'.

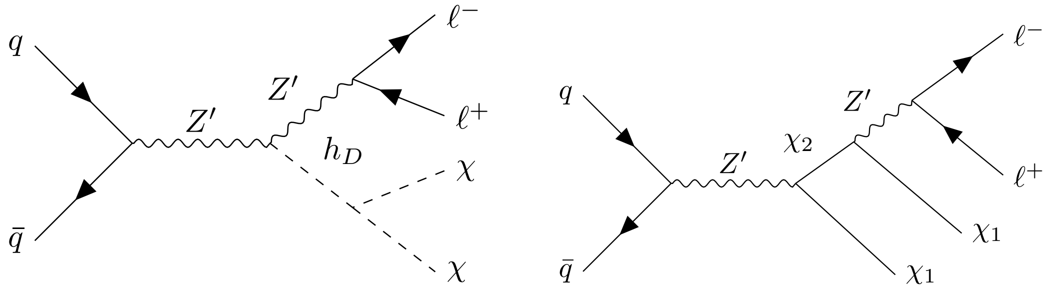

(a) (b)

Figure 1: Feynman diagrams for Z' production and leptonic decay in association with missing transverse energy in (a) the dark-Higgs and (b) the light-vector model.

Both models have six free parameters: the masses of the Z' and the dark-sector particles, as well as relevant couplings of the Z' to other particles. In each model there are two dark-sector particles: h_{D} and χ in the dark-Higgs model and χ_1 and χ_2 in the light-vector model. Following recommendations in Ref. [1], two benchmark scenarios are considered for each model: the heavy and the light dark-sector. The parameters

Table 1: The mass parameters assumed in the light dark-sector and heavy dark-sector benchmark scenarios [1].

	Dark Higgs	Light Vector
Light dark-sector	$m_\chi = 5$ GeV	$m_{\chi_1} = 5$ GeV
	$m_{h_\mathrm{D}} = 125$ GeV	$m_{\chi_2} = m_{\chi_1} + m_{Z'} + 25$ GeV
Heavy dark-sector	$m_\chi = 5$ GeV	$m_{\chi_1} = m_{Z'}/2$
	$m_{h_\mathrm{D}} = m_{Z'}$	$m_{\chi_2} = 2m_{Z'}$

assumed for this study are consistent with those used in the hadronic Z' search [4] and are summarized in Table 1. The search is performed for Z' masses above 200 GeV.

There are three coupling parameters considered in each model referring to the coupling of the Z' to quarks (g_q), to leptons (g_ℓ), and to the dark-sector particles (g_{DM}). In the dark-Higgs model the coupling g_{DM} is the coupling between the Z' and h_D while in the light-vector model g_{DM} is the coupling between Z' and the dark-sector particles χ_1 and χ_2. The couplings to quarks and leptons are assumed to be constant across generations. The couplings for this search are set to $g_{DM} = 1$, $g_q = 0.1$, and $g_\ell = 0.01$. The values for g_{DM} and g_q are taken to be the same as in Ref. [4], with non-zero g_ℓ introduced to allow the leptonic decay of the Z' boson. This choice follows the recommendation of the LHC Dark Matter Working Group [6]. The factor of ten difference between g_q and g_ℓ could be explained by a Z' coupling only to quarks at tree-level, with leptonic couplings generated through higher-order corrections.

The rest of this note is organized as follows. A brief introduction to the ATLAS detector is given in Section 2. In Section 3 the data and simulated signal and background event samples are described. The algorithms for the reconstruction and identification of final state particles are summarized in Section 4. The analysis strategy is detailed in Section 5, including the criteria for the selection of signal candidates and the estimation of SM backgrounds. The uncertainties that are taken into account in the statistical interpretation of data are described in Section 6. An overview of the statistical analysis and framework is given in Section 7. Finally the results are presented in Section 8 with concluding remarks given in Section 9.

2 ATLAS detector

The ATLAS experiment [7] at the LHC is a multipurpose particle detector with a forward–backward symmetric cylindrical geometry and a near 4π coverage in solid angle.[1] It consists of an inner tracking detector surrounded by a thin superconducting solenoid providing a 2 T axial magnetic field, electromagnetic and hadron calorimeters, and a muon spectrometer. The inner tracking detector covers the pseudorapidity range $|\eta| < 2.5$. It consists of silicon pixel, silicon microstrip, and transition radiation tracking detectors. Lead/liquid-argon (LAr) sampling calorimeters provide electromagnetic (EM) energy measurements with high granularity for $|\eta| < 3.2$. A steel/scintillator-tile hadron calorimeter covers the central pseudorapidity range ($|\eta| < 1.7$). The endcap and forward regions are instrumented with LAr calorimeters for both the EM and hadronic energy measurements up to $|\eta| = 4.9$. The muon spectrometer surrounds the calorimeters

---

[1] ATLAS uses a right-handed coordinate system with its origin at the nominal interaction point (IP) in the centre of the detector and the z-axis along the beam pipe. The x-axis points from the IP to the centre of the LHC ring, and the y-axis points upwards. Polar coordinates (r, ϕ) are used in the transverse plane, ϕ being the azimuthal angle around the z-axis. The pseudorapidity is defined in terms of the polar angle θ as $\eta = -\ln\tan(\theta/2)$. Angular distance is measured in units of $\Delta R \equiv \sqrt{(\Delta\eta)^2 + (\Delta\phi)^2}$.

and is based on three large superconducting air-core toroidal magnets with eight coils each. The field integral of the toroids ranges between 2.0 and 6.0 T m across most of the detector. The muon spectrometer includes a system of precision tracking chambers and fast detectors for triggering. A two-level trigger system is used to select events. The first-level trigger is implemented in hardware and uses a subset of the detector information to accept events at a rate below 100 kHz. This is followed by a software-based trigger that reduces the accepted event rate to 1 kHz on average depending on the data-taking conditions. An extensive software suite [8] is used in data simulation, in the reconstruction and analysis of real and simulated data, in detector operations, and in the trigger and data acquisition systems of the experiment.

3 Data and simulated event samples

The dataset used in this analysis was collected during LHC Run 2 in stable beam conditions and with all detector systems operating normally. The event quality was checked to remove events with noise bursts or coherent noise in the calorimeters. Events in the dielectron channel were recorded using a dielectron trigger [9] based on the 'very loose' or 'loose' identification criteria with transverse energy (E_T) thresholds between 12 and 24 GeV for both electrons, depending on the data-taking period. Events in the dimuon channel are required to pass one of various dimuon triggers [10], with transverse momentum (p_{T}) thresholds between 18 and 22 GeV for the leading muon and 8 GeV for the sub-leading muon or two muons above 10 GeV and 14 GeV, depending on the data-taking period. For events with different lepton flavours $e^{\pm}\mu^{\mp}$, various dilepton triggers are combined depending on the leading and sub-leading lepton flavour and data-taking period. After considering the data-quality requirements, to ensure that all parts of the detector were operational, the total data sample amounts to an integrated luminosity of 140 fb^{-1} [11], with an uncertainty of 0.83% [12], obtained using the LUCID-2 detector [13] for the primary luminosity measurements, complemented by measurements using the inner detector and calorimeters.

All signal and background processes from hard-scatter pp collisions were modelled by simulating the detector response to particles produced with Monte Carlo (MC) event generators. For the background processes the detector response was simulated using the full modelling of the ATLAS detector [14] in GEANT4 [15]. The signal MC samples were processed with a fast simulation [14] which relies on a parameterisation of the calorimeter response [16]. The effect of multiple pp interactions in the same or neighbouring bunch crossing (pileup) was modeled by overlaying the simulated hard-scattering event with inelastic events generated with Pythia 8.186 [17] using the NNPDF2.3lo set of parton distribution functions (PDF) [18] and the A3 set of tuned parameters [19]. The simulated events were weighted to reproduce the distribution of the average pileup observed in the data.

Table 2 shows a summary of the simulated event samples used to model the SM background in the analysis. It lists the matrix element and parton shower generators, the order of the cross section computation in the strong coupling constant, α_{s}, used to normalize the event yield, the sets of underlying-event and hadronization parameter values (tuned parameters of the MC program) for the parton shower and the PDF sets used by the generators.

Backgrounds due to top-quark pair- and single production are generated with Powheg-Box v2 [23] using the NNPDF3.0nlo PDF set, interfaced to Pythia 8 [24] for the parton shower and hadronization.

The diboson background is generated with Sherpa 2.2.11 [37] for semi-leptonic and Sherpa 2.2.12 for fully leptonic final states, using the NNPDF3.0nnlo PDF set [33].

Table 2: Simulated background event samples with the corresponding matrix element and parton shower (PS) generators, cross section order in α_s used to normalize the event yield, underlying-event tune and the PDF sets used. For boson and diboson samples V refers to the W or Z boson. 'Default' refers to the the default tune in the SHERPA generator.

Physics process	Generator	Parton shower	Normalization	Tune	PDF (generator)	PDF (PS)
$t\bar{t}$	POWHEG BOX v2 [20–23]	PYTHIA 8.230 [24]	NNLO+NNLL [25–31]	A14 [32]	NNPDF3.0NLO [33]	NNPDF2.3LO [18]
Single-top	POWHEG BOX v2 [21–23, 34]	PYTHIA 8.230 [24]	NLO+NNLL [35, 36]	A14 [32]	NNPDF3.0NLO [33]	NNPDF2.3LO [18]
Diboson VV	SHERPA 2.2.11, 2.2.12 [37]	SHERPA 2.2.11, 2.2.12 [38, 39]	NLO [40–43]	Default [44]	NNPDF3.0NNLO [33]	NNPDF3.0NNLO [33]
$Z/\gamma^*(\rightarrow \ell\ell)$+jets	SHERPA 2.2.11 [37]	SHERPA 2.2.11 [39]	NNLO [45]	Default [44]	NNPDF3.0NNLO [33]	NNPDF3.0NNLO [33]
$V(\rightarrow \ell\ell) + \gamma$	SHERPA 2.2.11 [37]	SHERPA 2.2.11 [39]	NNLO [45]	Default [44]	NNPDF3.0NNLO [33]	NNPDF3.0NNLO [33]
Signal	MADGRAPH v2.9.9 [46]	PYTHIA 8.306 [47]	LO	A14 [32]	NNPDF2.3LO [18]	NNPDF2.3LO [18]

The background from the neutral current Drell-Yan (DY) process $Z/\gamma^* \rightarrow \ell\ell$ (with $\ell = e, \mu, \tau$) is simulated with SHERPA 2.2.11 using the NNPDF3.0NNLO set [33]. The Sherpa generator is used instead of the Powheg generator from the previous ATLAS inclusive dilepton search [2] due to better modelling of the additional event activity, which is crucial for the final state considered in this analysis. The DY event yields are corrected with a rescaling that depends on the dilepton invariant mass from NLO to next-to-next-to-leading order (NNLO) in α_s, computed with VRAP 0.9 [48] and the CT14NNLO PDF set [49]. Mass-dependent electroweak corrections were computed at NLO with MCSANC 1.20 [50].

Signal MC samples are generated for Z' decaying either to dielectrons or dimuons in the four benchmark scenarios shown in Table 1 and discussed in Section 1. These samples are generated with MADGRAPH v2.9.9 [46] in the mass range of Z' between 200 GeV and 1000 GeV in steps of 100 GeV, using the NNPDF2.3LO PDF set and A14 [32] tune, interfaced to PYTHIA 8.306 for the parton shower and hadronization. The signal MC samples are generated with the couplings set to the nominal values as discussed in Section 1 ($g_{DM} = 1$, $g_q = 0.1$, and $g_\ell = 0.01$). The small coupling to leptons drastically reduces the cross section for the signal processes under consideration. However, these sample cross sections can be rescaled to different coupling values assuming the final state kinematics are not significantly altered. In particular, when scaling the leptonic coupling up by a factor of 10 it was found that the width over mass of the Z' varies by at most 20% of its original value of below 0.5% in all signal models considered in this note.

4 Object definitions

The leptons used in this analysis undergo two levels of selection criteria. The first selection, baseline leptons, consists of less stringent requirements on the quality of the leptons. This definition is used in the calculation of missing transverse momentum as well as the data-driven fake and non-prompt (FNP) background estimation described in Section 5. The more stringent selection, signal leptons, are used for the final event selection.

Electron candidates are reconstructed using energy clusters in the EM calorimeter which are matched to an inner detector track, and they are calibrated as described in Ref. [51]. Baseline electron candidates are required to have $|\eta| < 2.47$ in order to pass through the fine-granularity region of the EM calorimeter and be outside the range $1.37 < |\eta| < 1.52$ corresponding to the transition region between the barrel and endcap EM calorimeters. They should also satisfy 'loose' identification criteria and have $p_T > 25$ GeV. The trajectory of baseline electrons must be consistent with the primary vertex to suppress electrons originating from pileup. Therefore, the tracks associated with baseline electrons must have a longitudinal impact parameter relative to the primary vertex (z_0) such that $|z_0 \cdot \sin\theta| < 0.5$ mm and a transverse impact parameter significance $|d_0/\sigma(d_0)| \leq 5$. Signal electrons are defined as baseline candidates that satisfy the 'medium' identification and 'tight' isolation requirements [51].

Baseline muon candidates are reconstructed in the region $|\eta| < 2.5$ by matching inner detector tracks to tracks reconstructed in the muon spectrometer, and they are calibrated in situ using $Z \rightarrow \mu\mu$ decays [52]. Baseline muon candidates are required to have $p_{\mathrm{T}} > 25$ GeV. They have to satisfy a set of requirements on the quality of the tracks defined as 'high-pt' [52] and to pass requirements on the longitudinal impact parameter $|z_0 \cdot \sin\theta| < 0.5$ mm and significance of transverse impact parameter $|d_0/\sigma(d_0)| \leq 3$. Signal muons need to pass the 'tightTrackOnly' muon identification requirement [52].

The particle flow algorithm [53] using the anti-k_t algorithm [54] with a radius parameter of $R = 0.4$ is used to reconstruct jets with a four-momentum recombination scheme, using three-dimensional clusters of energy in the calorimeter [55] as inputs. Jets are then calibrated as described in Ref. [56, 57]. Events are vetoed if they contain jets induced by calorimeter noise or non-collision background, according to criteria described in Ref. [58], which has an efficiency of selecting jets from pp collision of > 99.5% for jets with $p_{\mathrm{T}} > 20$ GeV. Jets are further required to have $p_{\mathrm{T}} > 20$ GeV and $|\eta| < 4.5$. Additional jets that arise from pileup interactions are rejected by applying a dedicated 'tight' track-based selection Jet Vertex Tagger [59] for jets in $|\eta| < 2.5$, based on classifying the tracks associated with the jet as pointing or not pointing to the primary vertex. For the forward jets, $2.5 < |\eta| < 4.5$, a 'tight' selection of the forward Jet Vertex Tagger [60] is used.

Jets containing b-flavoured hadrons (b-jets) are identified with the `DL1r` algorithm, using a fully connected multi-layer feed-forward neural network [61, 62]. A jet is considered a b-jet candidate if it passes a requirement of the `DL1r` algorithm corresponding to an average efficiency of 85% to identify b-jets, evaluated with the $t\bar{t}$ MC used to train the algorithm. Any event containing at least one b-jet candidate passing the 'tight' Jet Vertex Tagger requirement with $p_{\mathrm{T}} > 20$ GeV and $|\eta| < 2.5$ is vetoed.

The reconstruction of the same energy deposits as multiple objects is resolved following the procedure outlined in Table 3. The steps are performed in listed order and only surviving objects participate in the subsequent steps.

Table 3: Overview of the overlap removal procedure and the corresponding matching criteria. The steps are performed in listed order and only surviving objects participate in the subsequent steps.

Reject	Against	Criteria
Muon	Electron	muon with calorimeter deposits and shared inner detector track
Jet	Electron	$\Delta R < 0.2$
Jet	Muon	(number of tracks < 3 or $p_{\mathrm{T}}^{\mathrm{jet}} < 100 p_{\mathrm{T}}^{\mu}$) and (ghost-associated [63] or $\Delta R < 0.2$)

The missing transverse momentum, $\mathbf{p}_{\mathrm{T}}^{\mathrm{miss}}$, is calculated from the negative vector sum of the transverse momenta of all baseline objects considered in the analysis [64]. Low-momentum tracks from the primary vertex and calorimeter clusters that are not associated with reconstructed analysis objects are also included in the calculation. The magnitude of $\mathbf{p}_{\mathrm{T}}^{\mathrm{miss}}$ is denoted by $E_{\mathrm{T}}^{\mathrm{miss}}$. Additionally, an object-based $E_{\mathrm{T}}^{\mathrm{miss}}$ significance ($E_{\mathrm{T}}^{\mathrm{miss,sig}}$) [65] is adopted in the analysis to help discriminate between events where $E_{\mathrm{T}}^{\mathrm{miss}}$ arises from undetected particles in the final state from those where it stems from limited $\mathbf{p}_{\mathrm{T}}$ resolution and identification inefficiencies. The $E_{\mathrm{T}}^{\mathrm{miss}}$ significance is defined by

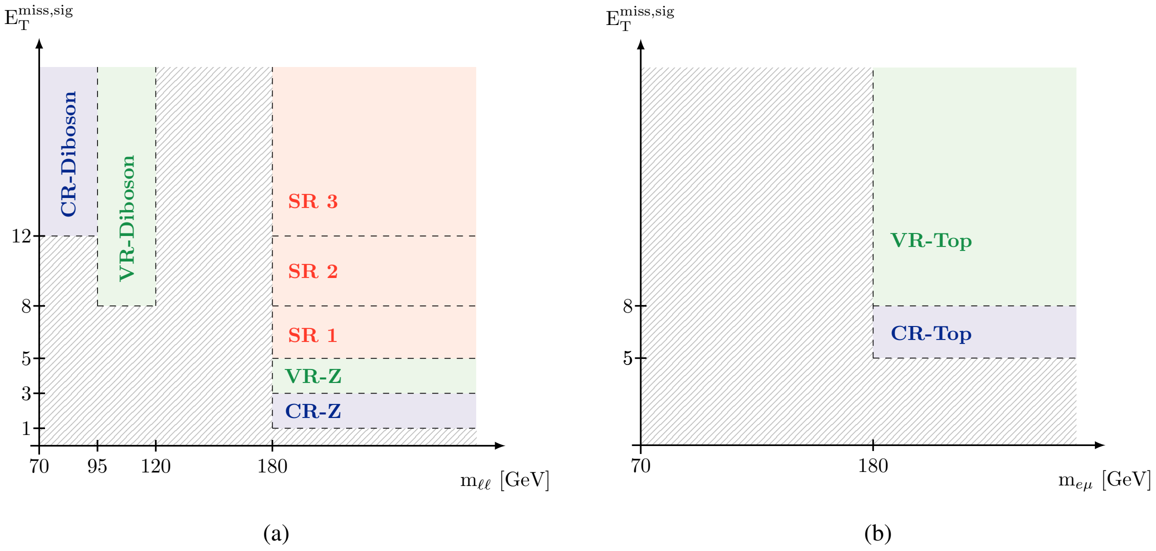

Figure 2: An overview of the analysis strategy shown in the m_{ll}-$E_T^{\text{miss,sig}}$ plane for the (a) same flavour lepton selection and (b) different flavour lepton selection.

$$E_{\mathrm{T}}^{\text{miss,sig}} = \frac{|\mathbf{p}_{\mathrm{T}}^{\text{miss}}|}{\sqrt{\sigma_{\mathrm{L}}^2(1-\rho_{\mathrm{LT}}^2)}}$$

where σ_{L} is the longitudinal component of the total transverse momentum resolution for all objects in the event while ρ_{LT} is the correlation factor between the parallel and perpendicular components of the transverse momentum resolution for each object [65].

Correction factors derived from data are applied to the simulated event samples on an event-by-event basis to account for differences between data and simulation in the lepton, jet and $E_{\mathrm{T}}^{\text{miss}}$ reconstruction efficiencies, energy scales and resolutions as well as in the lepton trigger and jet flavor tagging efficiency [51, 52, 61].

5 Event selection and background estimation strategy

Events are required to have a primary vertex, defined as the pp interaction vertex candidate with the highest sum of the squared transverse momenta of all associated tracks with $p_{\mathrm{T}} > 400$ MeV [66]. Only events with a primary vertex with at least two associated tracks are selected. Further, the events are required to have exactly two oppositely charged signal leptons. Only events with two light leptons of same flavour (SF), i.e. $e^{\pm}e^{\mp}$ and $\mu^{\pm}\mu^{\mp}$, are considered for the signal regions. However, events with different flavour (DF) light leptons, i.e. $e^{\pm}\mu^{\mp}$, are used in the evaluation of backgrounds from processes involving top quarks. Events passing the same criteria as described above, except that the quality requirement of the leptons is relaxed to the baseline selection, are used when estimating the contribution from the FNP background.

All signal scenarios considered in this analysis contain a resonant production of two leptons from a Z' produced in association with particles escaping detection and would only be observed indirectly through relatively large missing transverse energy in the event. Therefore, a selection of $E_{\mathrm{T}}^{\mathrm{miss}} > 55$ GeV is required. The two main discriminating variables used to build the signal regions (SRs) in this analysis are therefore the invariant mass of the dilepton pair m_{ll} and $E_{\mathrm{T}}^{\mathrm{miss,sig}}$. Since all of the signal models are targeting Z' masses well above the Z mass, a cut of $m_{ll} > 180$ GeV is applied to remove events with $Z \to \ell\ell$. In addition, a veto on events containing b-jets is applied to reduce the background from events involving top quarks. Having three orthogonal SRs covering different ranges of $E_{\mathrm{T}}^{\mathrm{miss,sig}}$ is found to increase the sensitivity of this search compared to a single SR, since several signal models with different predicted $E_{\mathrm{T}}^{\mathrm{miss}}$ distributions are targeted. The signal region bins are denoted as SR 1, SR 2, and SR 3 in order of increasing $E_{\mathrm{T}}^{\mathrm{miss,sig}}$. SR 1 is defined as $5 < E_{\mathrm{T}}^{\mathrm{miss,sig}} < 8$, SR 2 as $8 < E_{\mathrm{T}}^{\mathrm{miss,sig}} < 12$, and SR 3 as $E_{\mathrm{T}}^{\mathrm{miss,sig}} > 12$.

The SM backgrounds can be divided into two main categories: reducible and irreducible backgrounds. The irreducible backgrounds come from processes with prompt leptons which can yield events with a final state similar to the signal. The main irreducible backgrounds in this analysis come from processes with top quarks, dibosons, and Drell-Yan processes. These backgrounds are taken from MC simulation after normalization to data in dedicated control regions (CR) enriched in events containing the relevant processes. The normalization of the MC simulations are then validated in dedicated validation regions (VR). Both the CRs and VRs are constructed such that they are both similar and orthogonal to the signal regions, whilst also having little signal contamination, as illustrated in Figure 2(a) and Figure 2(b) for the SF and DF channel, respectively. This orthogonality is achieved by reverting either or both of the m_{ll} or $E_{\mathrm{T}}^{\mathrm{miss,sig}}$ cuts while keeping all the other cuts identical to the SR definitions. For the regions enriched in top quark processes, CR-Top and VR-Top, events with leptons of different flavour are used as this ensures a high purity of events containing top quarks while retaining the orthogonality to the SRs. The purity for the targeted backgrounds varies from > 93% in CR-Z to about 87-91% in the CR-Top and CR-Diboson.

The VRs are constructed to be more similar to the signal regions than the control regions in either $E_{\mathrm{T}}^{\mathrm{miss,sig}}$(VR-Z) or in m_{ll} (VR-Diboson). These regions are less pure in the targeted process than the corresponding CRs, but provide validation of the modelling of these processes in regions closer to the SRs. All of the regions defined remain orthogonal to each other, as illustrated by Figure 2.

The reducible backgrounds are processes where one or more of the leptons are classified as fake or non-prompt leptons and are estimated from data using the matrix method [67]. The matrix method uses two sets of leptons defined by the baseline and signal selection cuts presented in Section 4. A probability for a prompt lepton, which already passes the baseline selection to also pass the signal selection, is calculated as a function of both p_{T} and η using MC simulations after having applied all relevant correction factors. A similar probability for an FNP lepton to pass the signal selection when already having passed the baseline selection is measured in data as a function of p_{T} for muons[2] and p_{T} and η for electrons, using a control region (CR-Fakes) enhanced in FNP leptons. The CR-Fakes requirements are $|m_{ll} - m_Z| > 10$ GeV, $E_{\mathrm{T}}^{\mathrm{miss}} < 50$ GeV, and at least 1 b-tagged jet. It is also required that the transverse mass between the tagged lepton and the $E_{\mathrm{T}}^{\mathrm{miss}}$ is less than 50 GeV, $\Delta R(\ell_t, \text{b-jet}) < 0.3$, and $\Delta R(\ell_p, \text{jet}) > 0.4$. The final real efficiencies and fake rates are used as input to the matrix method together with the number of events containing either two baseline, one baseline and one signal, or two signal leptons in the region where the FNP background is to be estimated. To avoid double counting the contribution from FNP leptons in the analysis, all simulated events containing one or more FNP leptons are removed from the background samples. The FNP background estimates are validated in dedicated VRs requiring two same-sign (SS) leptons with $m_{ll} > 180$ GeV. In the electron channel an additional cut of $E_{\mathrm{T}}^{\mathrm{miss,sig}} > 5$ is applied to reduce the

---

[2] The η dependence of the muon fake rate is found to be almost flat and thus to enhance the statistics the fake rate is only derived as a function of p_{T}.

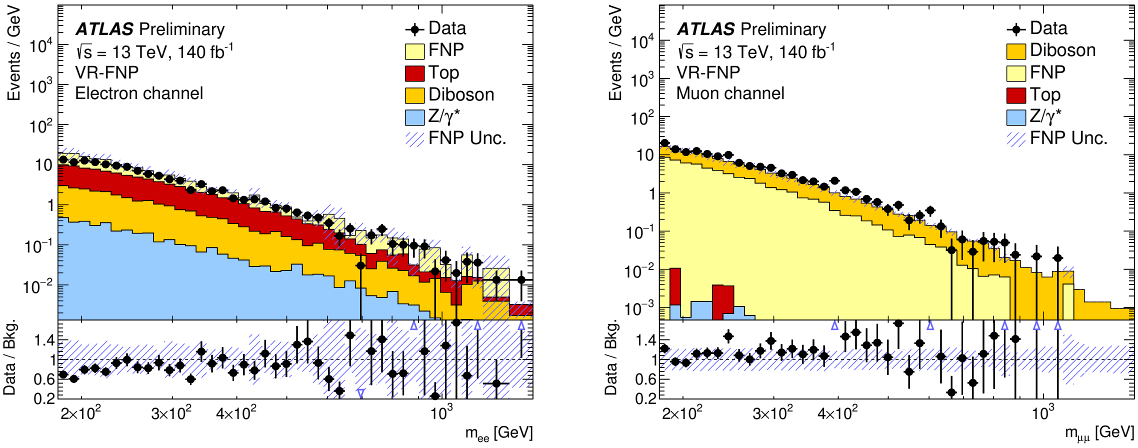

(a) (b)

Figure 3: Distributions of m_{ll} in the VR-FNP in the electron channel (a) and the muon channel (b). The leptons in this region are same-sign leptons. The uncertainty shown by the hatched band includes only the uncertainty from the matrix method itself. The last bin contains overflow events.

contribution from Z/γ^* events and FNP leptons coming from converted photons. The invariant mass of the SS dilepton pair in the VR-FNP is shown in Figures 3(a) and 3(b) for electrons and muons, respectively.

Due to the limited statistics at high $E_{\mathrm{T}}^{\mathrm{miss,sig}}$, the FNP background estimates obtained from the matrix method within the signal regions are parameterised as a function of m_{ll} in inclusive $E_{\mathrm{T}}^{\mathrm{miss,sig}}$ by fitting any array of functional forms to the data; similar to approaches used in Refs [68, 69]. A large list of functional forms were used initially, but several of them failed to explain the observed FNP estimates and were disregarded. For the functional forms found to have a satisfactory fit to the data-driven FNP estimates several permutations of the fit range in m_{ll} are tried, using combinations of 110 to 140 GeV for the minimum and 500 to 1000 GeV for the maximum. Additionally the number of bins used for the fitted distribution are varied between 10 to 80 bins. Each fit is then evaluated by studying the χ^2/ndf and by comparing the distribution of the pulls to a standard normal distribution. The selected nominal fits of the FNP estimates are all considering one of the following functional forms,

$$f_1 = (1 - m_{ll})^{\mathrm{p1}} * (m_{ll})^{(\mathrm{p2}+\mathrm{p3}*\log(m_{ll})+\mathrm{p4}*\log(m_{ll})^2)} \tag{1}$$

$$f_2 = e^{-p1}\,(m_{ll})^{p2}\,(m_{ll})^{p3*\log(m_{ll})} \tag{2}$$

$$f_3 = \frac{p1}{(m_{ll} + p2)^{p3}}, \tag{3}$$

where $p1$, $p2$, $p3$ and $p4$ are free parameters. An envelope of other functional forms using different fit ranges and number of bins are used to estimate the uncertainty on the extrapolation. Checks are performed in order to make sure that the fitted function and the cumulative distribution of the extrapolation reproduce the corresponding distribution of the data-driven FNP estimates at lower values of m_{ll}. Figure 4 shows the nominal fit function used to extrapolate the FNP estimates in a dielectron region with $5 < E_{\mathrm{T}}^{\mathrm{miss,sig}} < 8$ compared with the data-driven estimates obtained from the matrix method. The envelope uncertainty on the extrapolation is indicated by the hatched blue band. Different fit functions are used to extrapolate the FNP background estimates to high values of m_{ll} in the dielectron, dimuon, and eμ-channels. In the dimuon

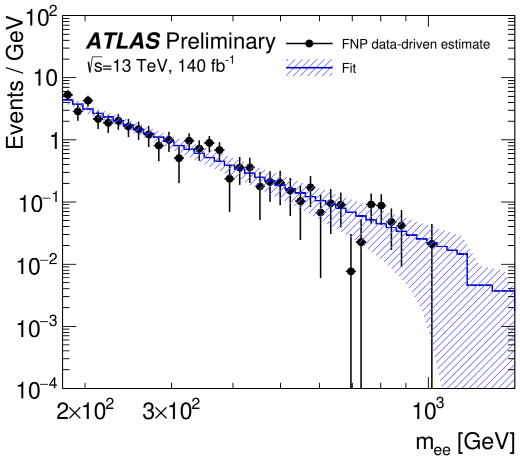

Figure 4: The nominal fit function used to extrapolate the FNP estimates as a function of m_{ll} in a region with $5 < E_{\mathrm{T}}^{\mathrm{miss,sig}} < 8$ for the dielectron channel compared with the data-driven estimates obtained from the matrix method in the same region. The envelope uncertainty of the extrapolation is indicated by the hatched blue band.

and eμ-channels the same functional form of Equation 1 is used to describe the FNP background in all regions of $E_{\mathrm{T}}^{\mathrm{miss,sig}}$. In the dielectron channel the functional forms in Equation 1, 2 and 3 are used in the low ($E_{\mathrm{T}}^{\mathrm{miss,sig}} < 5$), intermediate ($5 < E_{\mathrm{T}}^{\mathrm{miss,sig}} < 12$), and high ($E_{\mathrm{T}}^{\mathrm{miss,sig}} > 12$) $E_{\mathrm{T}}^{\mathrm{miss,sig}}$ regions, respectively.

6 Systematic uncertainties

The systematic uncertainties considered in this analysis are grouped into experimental uncertainties, theoretical uncertainties, and uncertainties from the data-driven FNP estimates. The systematic uncertainties for all background processes are found to be within 5% of the total background yields in all control and signal regions. The corresponding uncertainty on the FNP estimates lies between 0.2 - 3.3%. The experimental uncertainty, considering a light-vector signal model in the light dark-sector scenario with a Z' mass of 500 GeV, is between 5 and 7%. The largest uncertainty on the background comes from the FNP estimate, however this is a relatively minor background in all regions as shown in Tables 4 and 5.

6.1 Experimental uncertainties

The uncertainty on the integrated luminosity and pileup reweighting are applied as described in Section 3. Electron and muon uncertainties on the reconstruction [51, 52, 70], identification [52, 70], isolation and trigger efficiencies are considered together with the uncertainties on the energy scale and resolution. For jets, uncertainties from the jet vertex tagger [60], which account for the residual contamination from pileup jet, as well as the uncertainties from jet energy scale (JES) [57] and jet energy resolution (JER) [71], are considered. A total of 20 independent contributions are taken into account for the JES uncertainty and 13 independent contributions for the JER uncertainty. The uncertainties of flavor tagging are also considered [72–74]. The uncertainties on the objects used in the computation of $E_{\mathrm{T}}^{\mathrm{miss}}$ are propagated through the computation and constitute, together with additional uncertainties considering the scale and resolution of the contribution from low-momentum tracks not associated to any of the primary objects, the total uncertainty on $E_{\mathrm{T}}^{\mathrm{miss}}$.

6.2 Modelling uncertainties

The effect of initial- and final-state radiation uncertainties from the renormalization (μ_R) and factorization (μ_F) scales are estimated by considering several variations of μ_R and μ_F in the simulations. For the top backgrounds each of the two parameters are varied by a factor of 2 and 0.5 with respect to the nominal. For the Drell-Yan and diboson backgrounds a set of seven different permutations of μ_R and μ_F are used, where all possible permutations of 0.5, 1 and 2 times the nominal value for each scale are considered. The final uncertainty from the renormalization and factorization scales is taken as the envelope of all the variations.

For the Drell-Yan and diboson backgrounds the uncertainty from the PDFs are included by using the weights corresponding to the NNPDF3.0nnlo set with 100 replicas. These 100 variations are combined into one single uncertainty by calculating the standard deviation with respect to the nominal PDF. The effect on the PDF of varying α_S by ± 0.001 compared to the nominal value of $\alpha_S(m_Z) = 0.118$ is included by taking the average of the up and down variations and adding them in quadrature with the total PDF uncertainty. For the top quark background 30 systematic variations associated with the PDF4LHC15nlo set are used and compared to the PDF4LHC15nlo nominal prediction to obtain the corresponding relative variation.

To estimate the uncertainty coming from the re-summation and merging scale for the diboson and DY backgrounds dedicated samples are generated with:

- the re-summation scale varied by a factor four larger and smaller compared to the nominal value of 1.
- the scale for calculating the overlap between jets from the matrix element and parton shower varied up (down) by 10 GeV (5 GeV) from the nominal value of 20 GeV.
- an alternative recoil scheme CSS_KIN_SCHEME=1 [75], as opposed to the nominal setting of CSS_KIN_SCHEME=0 [76], to estimate the uncertainty associated with the mismodelling of jet multiplicities larger than three.

The systematic uncertainty stemming from all of these variations are summed in quadrature and considered as one single uncertainty in the analysis.

The top quark production modelling uncertainties are estimated for both $t\bar{t}$ and Wt production independently by comparing the nominal (Powheg+Pythia8) sample to the one produced by an alternative generator (MadGraph5_aMC@NLO) and an alternative showering (Herwig 7). The uncertainties assigned to the interference between single-top Wt and $t\bar{t}$ production [77] is obtained by comparing diagram removal (DR) and diagram subtraction (DS) samples, modelled by Powheg+Pythia 8.

Uncertainties related to the matrix element (hard scattering), fragmentation/hadronization (non-perturbative) effects and the damping parameter, h_{damp}[3], are evaluated for the $t\bar{t}$ and single-top backgrounds using a set of dedicated samples generated with different generators and settings for these variations. The uncertainties from the hard scattering and fragmentation/hadronization use samples generated with

---

[3] The h_{damp} parameter is a re-summation damping factor and one of the parameters that controls the matching of Powheg matrix elements to the parton shower and thus effectively regulates the high-p_{T} radiation against which the $t\bar{t}$ system recoils.

aMC@NLO+Pythia8 and Powheg+Herwig7, respectively. The effects of the h_{damp} parameter on the $t\bar{t}$ background yields are estimated by using simulations generated with Powheg+Pythia 8 using $h_{damp} = 3.0\,m_t$, as opposed to the nominal sample, generated with $h_{damp} = 1.5\,m_t$, where m_t is the top-quark mass.

6.3 Uncertainties on the FNP estimates

The uncertainties coming from the matrix method, used to estimate the contribution from FNP leptons, are mainly coming from the measurement of the fake rates and real efficiencies in addition to the uncertainties related to the fitting and extrapolation of the final FNP estimates, discussed in Section 5. An uncertainty on the subtraction of the real lepton contamination in CR-Fakes used to extract the fake rate from data is estimated by shifting the amount of real leptons up and down by 10%. This variation was chosen as a conservative estimate on the uncertainties of the cross section and modelling of $t\bar{t}$ processes, the dominant source of real leptons in the fake control region. The limited statistics in CR-Fakes is also included as an uncertainty on the corresponding fake rate. Moreover, dedicated real efficiencies are calculated for each systematic variation of the relevant correction factors applied to the simulated event samples. For each variation of the fake rate and real efficiency discussed above dedicated estimates are carried out and the corresponding FNP prediction is compared to the nominal in order to estimate the uncertainty. Additionally there are uncertainties related to the fitting of the FNP distribution taking into account the use of several different fit functions, bin sizes used in the fitting, and the m_{ll} ranges of the fits. An envelope of different fit functions are used to estimate the total uncertainty on this method.

7 Statistical analysis

A search for dark-matter in events with two SF opposite-sign light leptons and $E_{\mathrm{T}}^{\mathrm{miss}}$ is performed through a profile log-likelihood fit [78] of binned m_{ll} distributions in dedicated SRs and CRs. Dielectron and dimuon channels are considered both as independent channels and in a combined approach, under a lepton-flavour universality assumption [79, 80].

Signal samples were simulated with a Z' mass spacing of 100 GeV, which is significantly larger than the detector mass resolution for dielectron and dimuon channels. In order to obtain signal m_{ll} distributions for the intermediate Z' mass values a morphing approach was used, based on the moment morphing function implemented in RooFit [81]. The signal regions contain 40 logarithmic bins in m_{ll} for both the dielectron and dimuon channels, and by using the simulated event samples a PDF was contructed and morphed to create 40 signal m_{ll} distributions, each having the Z' mass set to the the central value of the corresponding SR bin. For the light dark-sector scenario in the dark-Higgs model only the simulated event samples are used, while the morphed samples are used for all the other signal models.

The statistical interpretation is performed using profile likelihood fits utilizing the RooFit [82] and RooStats [83] statistical analysis tools. The statistical models used are built following the HistFactory [84] approach. The likelihood function is a product of the probability density functions of the binned m_{ll} distributions in each region contributing to the fit. The number of events in each of the bins in the given regions is described using a Poisson distribution, the mean of which is the sum of the expected contributions from all background and signal sources. The uncertainties on the simulated event samples described in Section 6 are added into the fit as nuisance parameters in the likelihood using Gaussian constraints. All the experimental uncertainties are correlated between processes and regions included in the simultaneous profile likelihood fit. Normalization factors for the three main backgrounds; DY, diboson, and top quark pair- and single production, are considered together with all the nuisance parameters and adjusted by maximizing the likelihood. Moreover, the signal strength parameter, μ, is required to be ≥ 0 in the fit.

The significance of a discrepancy in the observed data compared with the expected SM background is given by a p-value, interpreted as the probability of observing such a discrepancy (or more extreme) assuming that no signal is present. The local p-value of the background-only hypothesis (p_0) is determined from a profile-likelihood-ratio-test statistic [78]. Upper limits at the 95% confidence level (CL) are evaluated with the modified frequentist $\mathrm{CL_S}$ method [85] using the asymptotic approximation to the test-statistic distribution [78].

8 Results and interpretation

A comparison of the distributions of observed and expected yields in the CRs and VRs after a simultaneous background-only profile log-likelihood fit [78] of the CRs and SRs under the assumption of no signal in the data is shown in Figures 5–7. Figure 5 shows the invariant mass distribution in CR-Z and VR-Z regions for electrons and muons. Figure 6 shows the corresponding DF invariant mass distribution in the CR-Top and VR-Top regions. Since the background-only fit is performed using a top control region requiring DF leptons the m_{ll} distributions used in the fits for electrons and muons are identical. Figure 7 shows the distribution of $E_{\mathrm{T}}^{\mathrm{miss,sig}}$ in the CR- and VR-Diboson regions for dielectron and dimuon events. The irreducible background predictions obtained from the fit are compared with data in the VRs to asses the quality of the background modelling. Normalization factors of 0.92 ± 0.03 (0.94 ± 0.03), 1.05 ± 0.06 (1.09 ± 0.07), and 0.99 ± 0.02 (0.98 ± 0.02) are obtained in the electron (muon) channel for the $t\bar{t}$ and single-top, diboson, and $Z/\gamma^*(\rightarrow \ell\ell)$+jets backgrounds, respectively. The quoted uncertainties include both statistical and systematic uncertainties.

The $m_{\ell\ell}$ distributions in the three SRs are shown in Figures 8 and 9 for the electron and muon channel, respectively. The yields of the various SM background processes and data are detailed in Tables 4 and 5 for electrons and muons, respectively. The corresponding yields for a light-vector model considering the light dark-sector scenario with $m_{Z'} = 500$ GeV are displayed in the table as an example.

Table 4: The number of observed data events and expected background contribution for the electron channel in all three SRs and the CRs. The expected yields for the light-vector model in the light dark-sector scenario with $m_{Z'} = 500$ GeV are also shown. The displayed yields include all sources of statistical and systematic uncertainties, but the individual uncertainties can be correlated or anticorrelated and thus the sum does not necessarily add up in quadrature.

	CR-Z	CR-Top	CR-Diboson	SR 1	SR 2	SR 3
Observed	125359	45003	1161	6508	2340	801
Total background	125 360 ± 350	45 010 ± 210	1158 ± 33	6490 ± 80	2370 ± 40	786 ± 20
Drell-Yan	118 700 ± 800	62.7 ± 2.0	60 ± 4	1100 ± 140	58 ± 4	14.9 ± 0.7
Top	2420 ± 180	40 600 ± 500	47 ± 5	3180 ± 210	1450 ± 90	379 ± 26
Diboson	2780 ± 140	3400 ± 170	1036 ± 34	1880 ± 90	750 ± 35	350 ± 15
FNP	1500 ± 600	900 ± 400	15.5 ± 2.5	330 ± 180	110 ± 70	41 ± 26
Signal, $m_{Z'} = 500$ GeV	0 ± 0	0 ± 0	0 ± 0	2.0 ± 2.0	2.2 ± 2.2	4 ± 4

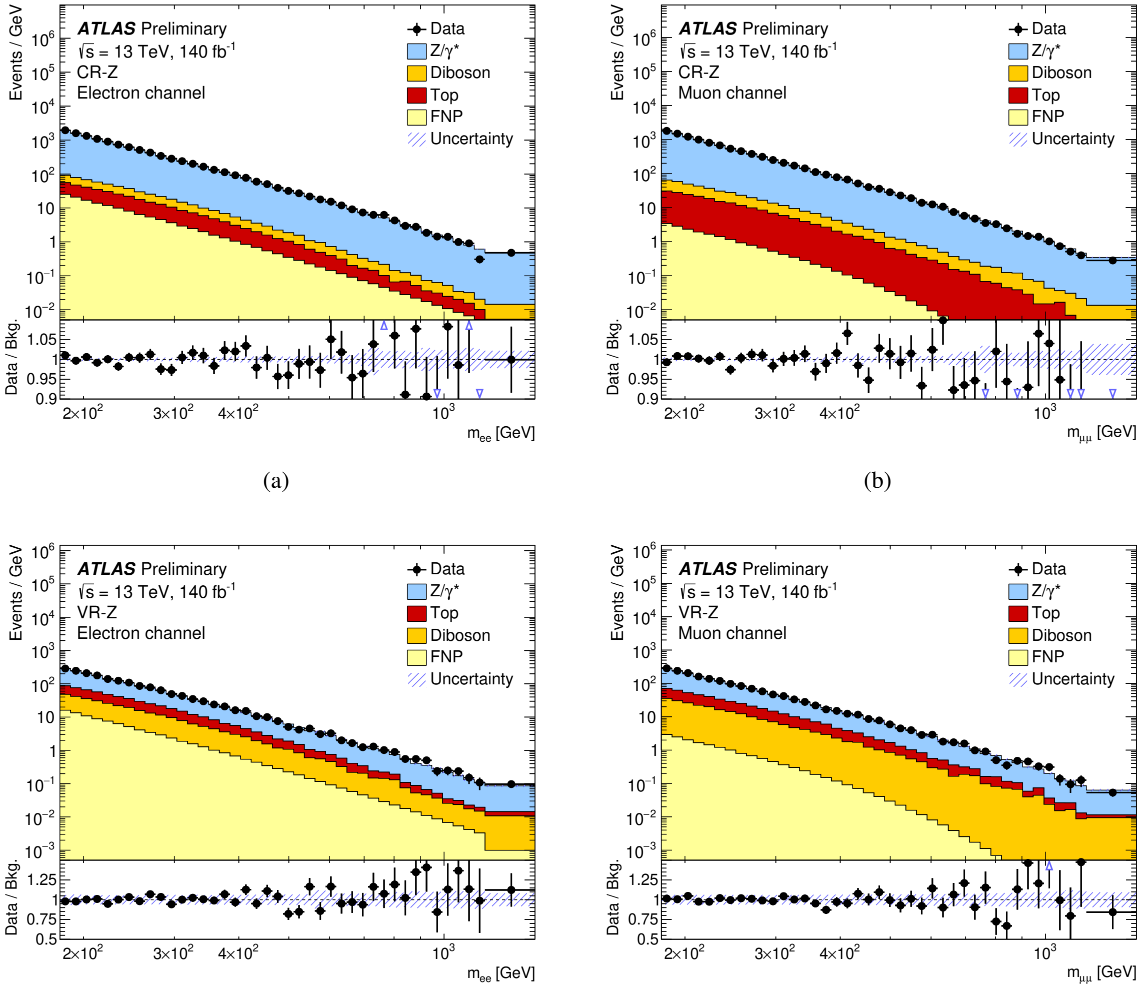

(a)

(b)

(c)

(d)

Figure 5: The $m_{\ell\ell}$ distribution in the CR-Z (a, b) and VR-Z (c, d) for the electron channel (a, c) and muon channel (b, d) after the background predictions have been normalized according to the background-only fit. The total uncertainty on the SM background is shown by the hatched band and it includes both statistical and systematic uncertainties. The ratio of the observed and expected yields is shown in the lower panels. The last bin contains overflow events.

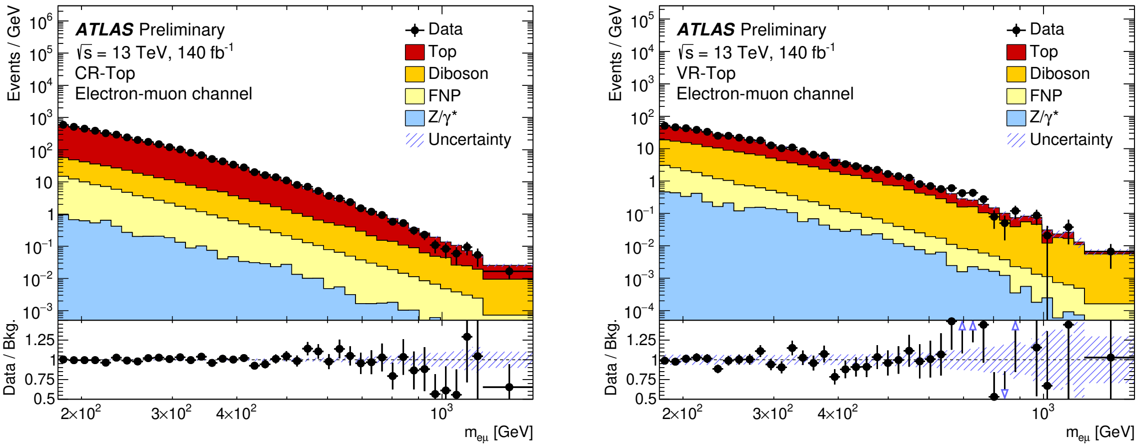

(a)

(b)

Figure 6: The $m_{\ell\ell}$ distribution of DF lepton pairs in CR-Top 6(a) and VR-Top 6(b). Since the background-only fit is performed using a control region requiring DF leptons the m_{ll} distributions used in the fits for electrons and muons are identical. The m_{ll} distribution in the validation region is therefore only shown after the full background-only fit in the electron channel (the distribution from the fit to the muon channel is identical). The total uncertainty on the SM background is shown by the hatched band and it includes both statistical and systematic uncertainties. The ratio of the observed and expected yields is shown in the lower panels. The last bin contains overflow events.

Table 5: The number of observed data events and expected background contribution for the muon channel in all three SRs and the CRs. The expected yields for the light-vector model in the light dark-sector scenario with $m_{Z'} = 500$ GeV are also shown. The displayed yields include all sources of statistical and systematic uncertainties, but the individual uncertainties can be correlated or anticorrelated and thus the sum does not necessarily add up in quadrature.

	CR-Z	CR-Top	CR-Diboson	SR 1	SR 2	SR 3
Observed	112334	45003	970	6566	2095	455
Total background	112 340 ± 340	45 000 ± 220	969 ± 30	6530 ± 80	2150 ± 40	437 ± 11
Drell-Yan	107 100 ± 400	62.7 ± 2.0	48 ± 17	1520 ± 160	125 ± 7	20.1 ± 0.6
Top	2330 ± 190	40 600 ± 500	45 ± 6	2980 ± 170	1310 ± 50	218 ± 11
Diboson	2610 ± 150	3550 ± 200	867 ± 35	1890 ± 90	669 ± 30	189 ± 9
FNP	240 ± 150	800 ± 400	9.0 ± 3.5	120 ± 90	38 ± 29	7 ± 7
Signal, $m_{Z'} = 500$ GeV	0 ± 0	0 ± 0	0 ± 0	8 ± 4	8 ± 4	9 ± 5

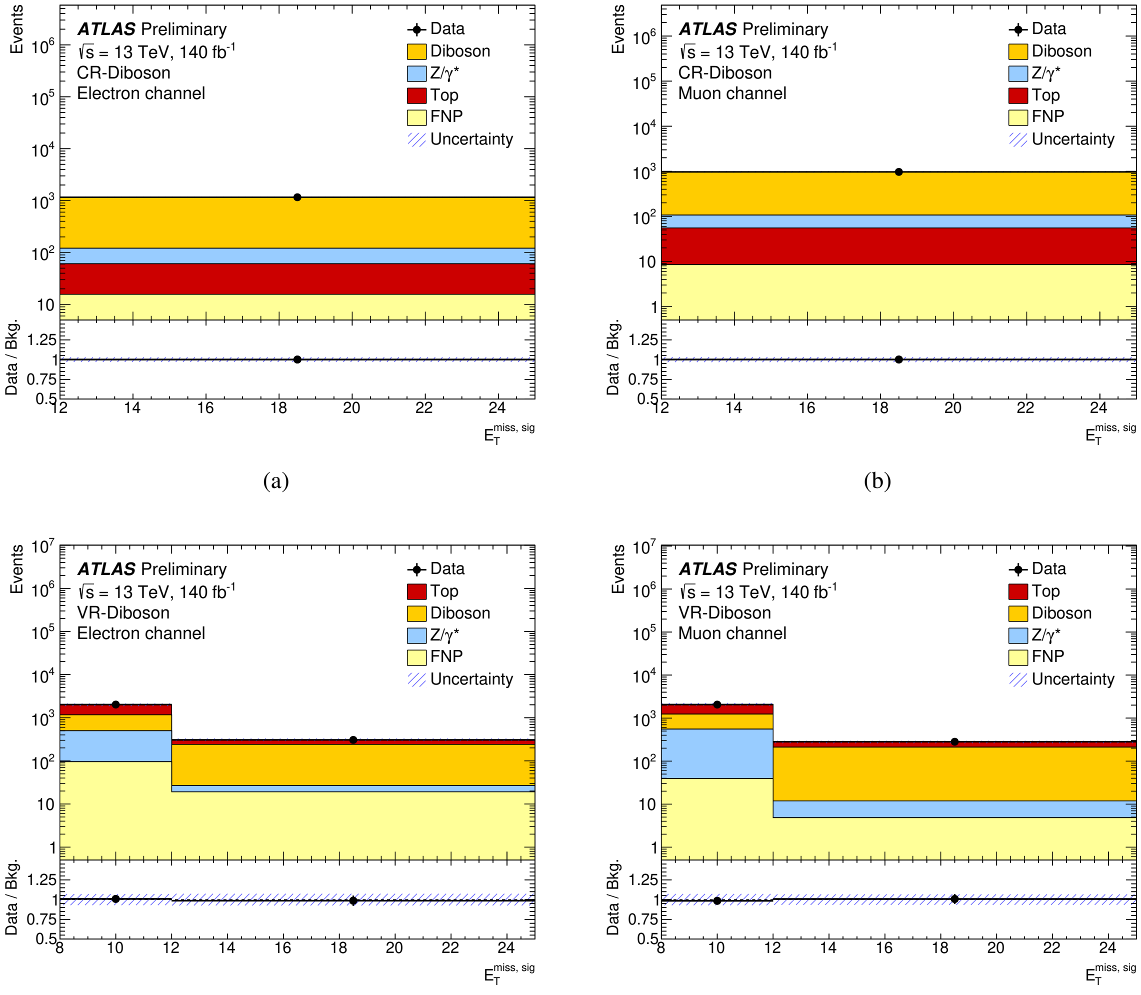

(a) (b)

(c) (d)

Figure 7: The $E_{\mathrm{T}}^{\mathrm{miss,sig}}$ distribution in CR-Diboson (a, b) and VR-Diboson (c, d) for the electron channel (a, c) and muon channel (b, d) after the background predictions have been normalized according to the background-only fit. The total uncertainty on the SM background is shown by the hatched band and it includes both statistical and systematic uncertainties. The ratio of the observed and expected yields is shown in the lower panels. Overflow events are included.

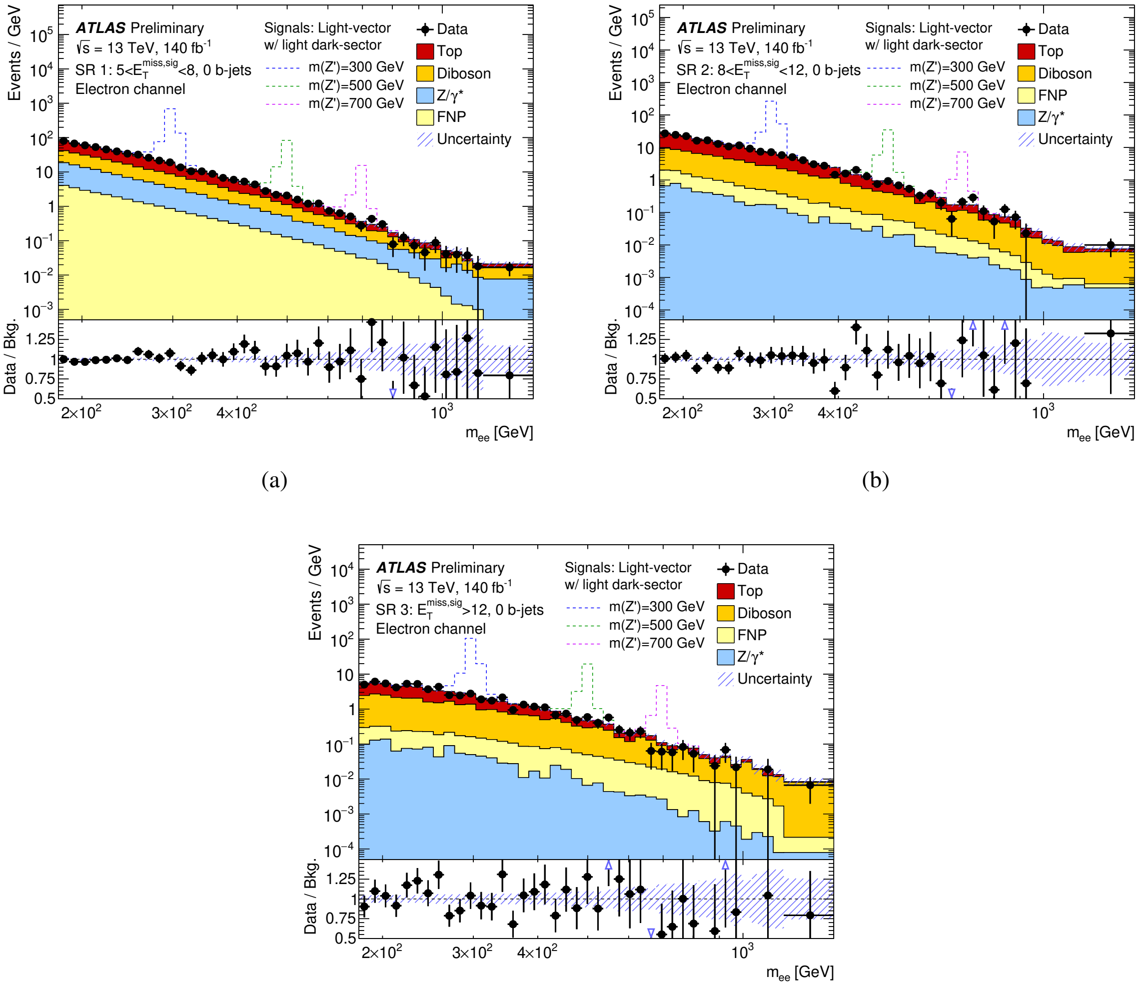

(a)

(b)

(c)

Figure 8: The $m_{\ell\ell}$ distribution in the electron channel for SR 1 ($5 < E_{\mathrm{T}}^{\mathrm{miss,sig}} < 8$) (a), SR 2 ($8 < E_{\mathrm{T}}^{\mathrm{miss,sig}} < 12$) (b) and SR 3 ($E_{\mathrm{T}}^{\mathrm{miss,sig}} > 12$) (c). The distributions are shown after performing a profile log-likelihood fit in the control and signal regions. The total uncertainty on the SM background is shown by the hatched band and it includes both statistical and systematic uncertainties. The last bin contains overflow events.

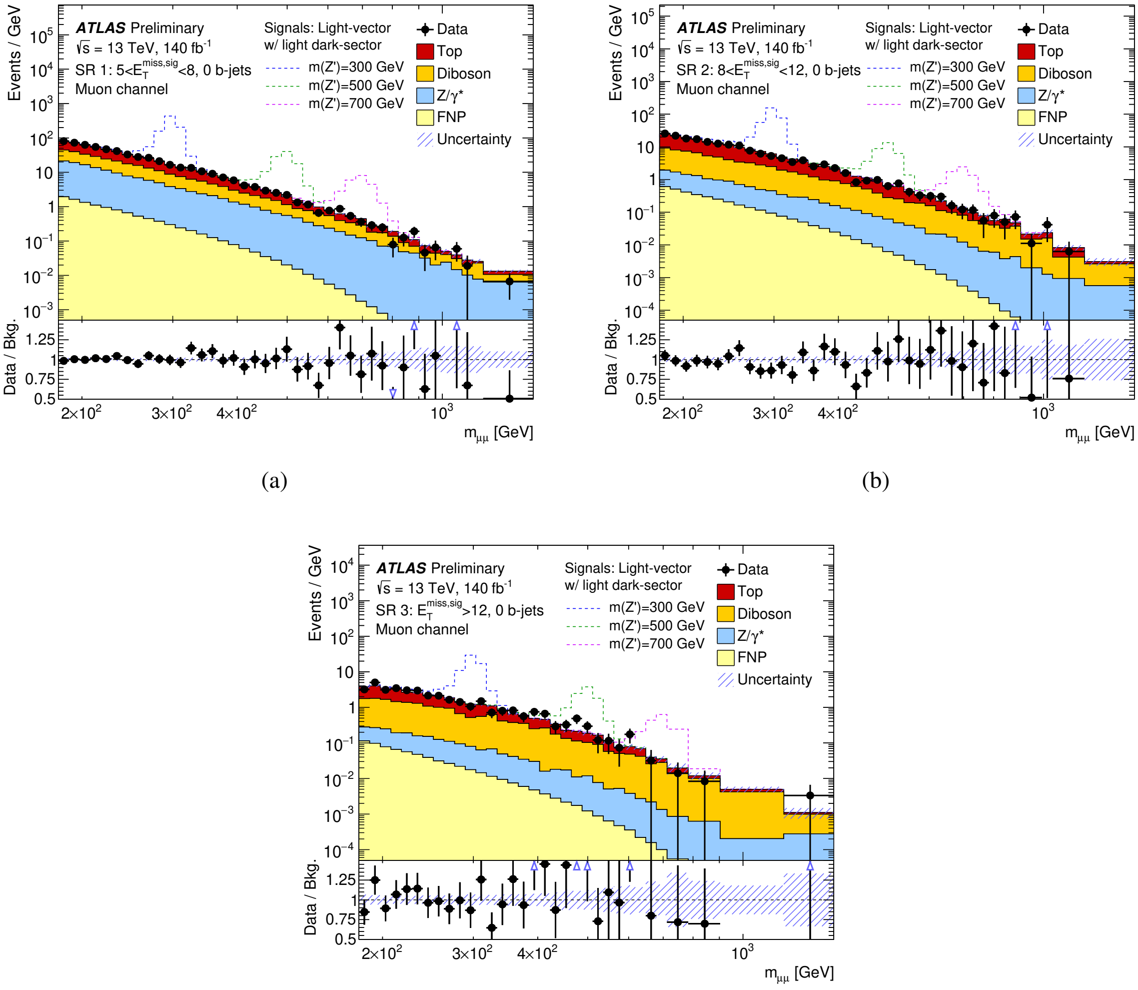

(a)

(b)

(c)

Figure 9: The $m_{\ell\ell}$ distribution in the muon channel for SR 1 ($5 < E_{\mathrm{T}}^{\mathrm{miss,sig}} < 8$) (a), SR 2 ($8 < E_{\mathrm{T}}^{\mathrm{miss,sig}} < 12$) (b) and SR 3 ($E_{\mathrm{T}}^{\mathrm{miss,sig}} > 12$) (c). The distributions are shown after performing a profile log-likelihood fit in the control and signal regions. The total uncertainty on the SM background is shown by the hatched band and it includes both statistical and systematic uncertainties. The last bin contains overflow events.

The probability that the data are compatible with the background-only hypothesis is shown in Figure 10, for the light-vector model in the light dark-sector scenario, as a function of $m_{Z'}$. The significance is obtained from a combination of the three signal regions. No significant deviation from the SM prediction is observed. In the e^+e^- channel there is a small excess around 275 GeV in all three signal regions shown in Figure 8 which combine to a local significance of 2.8 standard deviations (σ). The largest excess in the $\mu^+\mu^-$ channel is found around 470 GeV with a local significance of about 2.6σ, largely driven by SR 3 as shown in Figure 9(c), and is reduced in the combination of the electron and muon channels due to a deficit in the electron channel around the same mass. Similar results were achieved for other signal benchmark scenarios in this note.

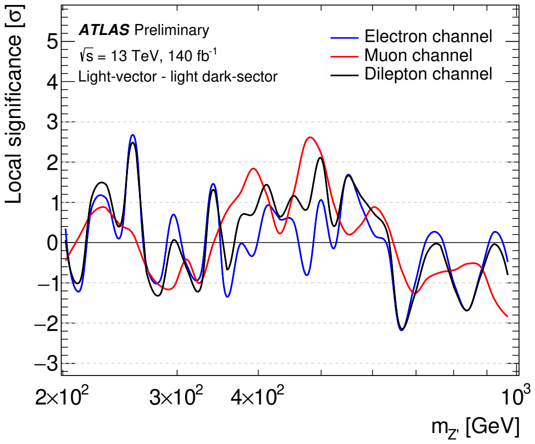

Figure 10: Local significance obtained when combining the results from the three SRs in the electron channel and muons channel separately, as well as for the combination (dilepton channel). The results are shown using the signal samples from the light-vector model considering the light dark-sector scenario.

In the absence of any significant excess above the SM background prediction cross section limits were set for all four scenarios: the light and heavy dark-sector scenarios in the dark-Higgs and light-vector models. Observed and expected cross section limits as a function of $m_{Z'}$ are shown in Figure 11 for the light-vector model, and Figure 12 for the dark-Higgs model. The limits shown here are obtained by combining the three SRs. These limits are presented for the electron and muon channels individually, as well as the for combined dilepton channel. As expected limits are more stringent in the heavy dark-sector scenarios due to their large $E_{\mathrm{T}}^{\mathrm{miss}}$ spectrum.

For all models it can be noted that none of the simulated signal points using a $Z'\ell\ell$ coupling of $g_\ell = 0.01$ are excluded. Thus theory curves for scenarios where the coupling g_ℓ is scaled up by a factor of 5 and 10, assuming the cross section to be proportional to g_ℓ^2, are shown in addition to the nominal coupling of 0.01. The other couplings in the model are fixed to their assigned values of $g_q = 0.1$ and $g_{DM} = 1$ for all cases.

Table 6 shows the obtained exclusion limits on cross section and lepton coupling at $m_{Z'} = 500$ GeV for all four benchmark models in both the electron and muon channel.

Furthermore, lepton coupling limits are extracted from the cross section limits. The observed limits on the lepton coupling are shown in Figures 13 and 14 for the light-vector and dark-Higgs models, respectively.

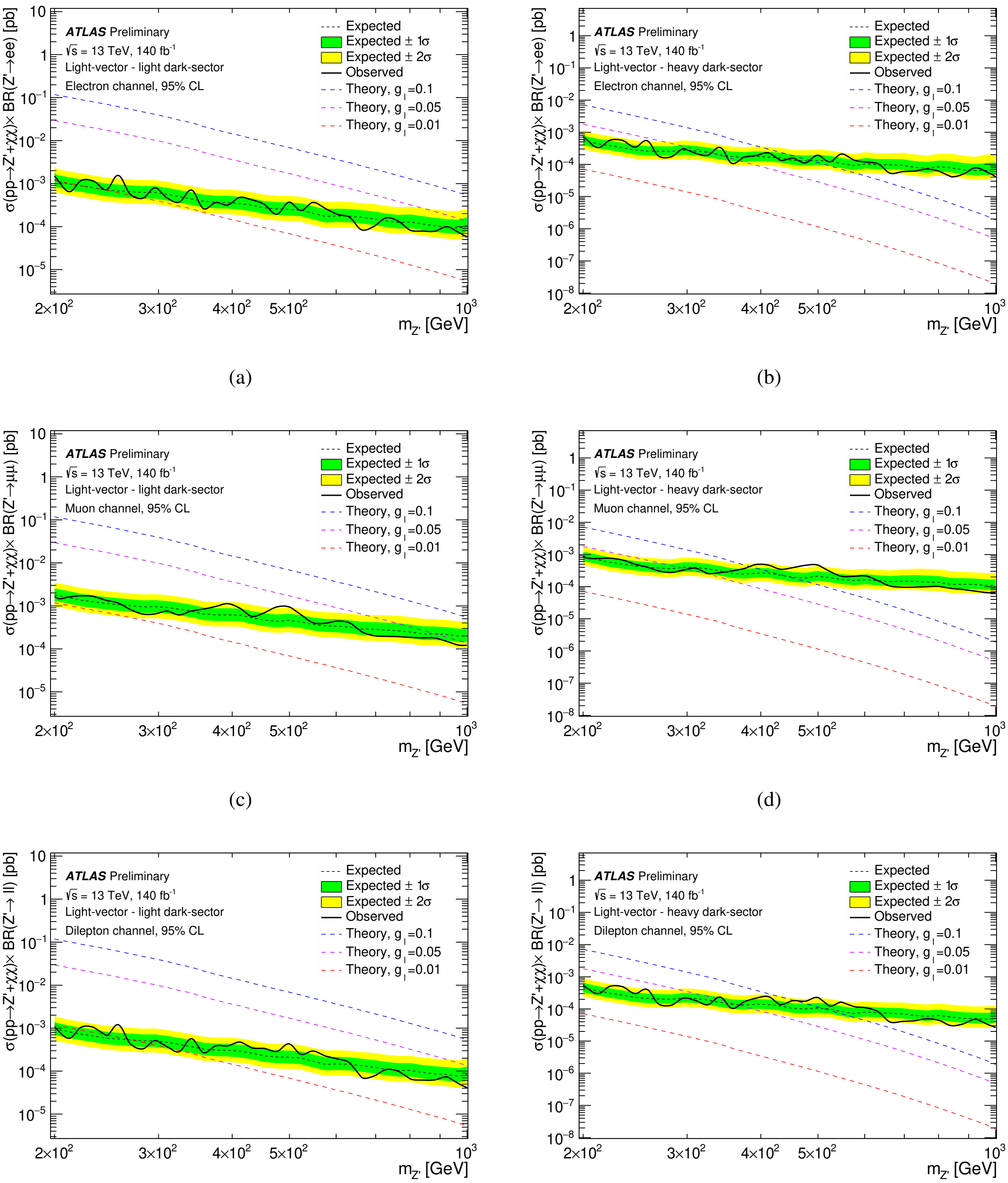

(a) (b)

(c) (d)

(e) (f)

Figure 11: Observed and expected cross section limits for the light-vector model with light dark-sector (left) and heavy dark-sector (right), shown for the electron channel (top), muon channel (middle) and the combined dilepton channel (bottom). The limits are obtained by combining the three SRs. The theory curves for $g_\ell = 0.05$ and $g_\ell = 0.1$ are obtained by assuming that the cross section scales as g_ℓ^2.

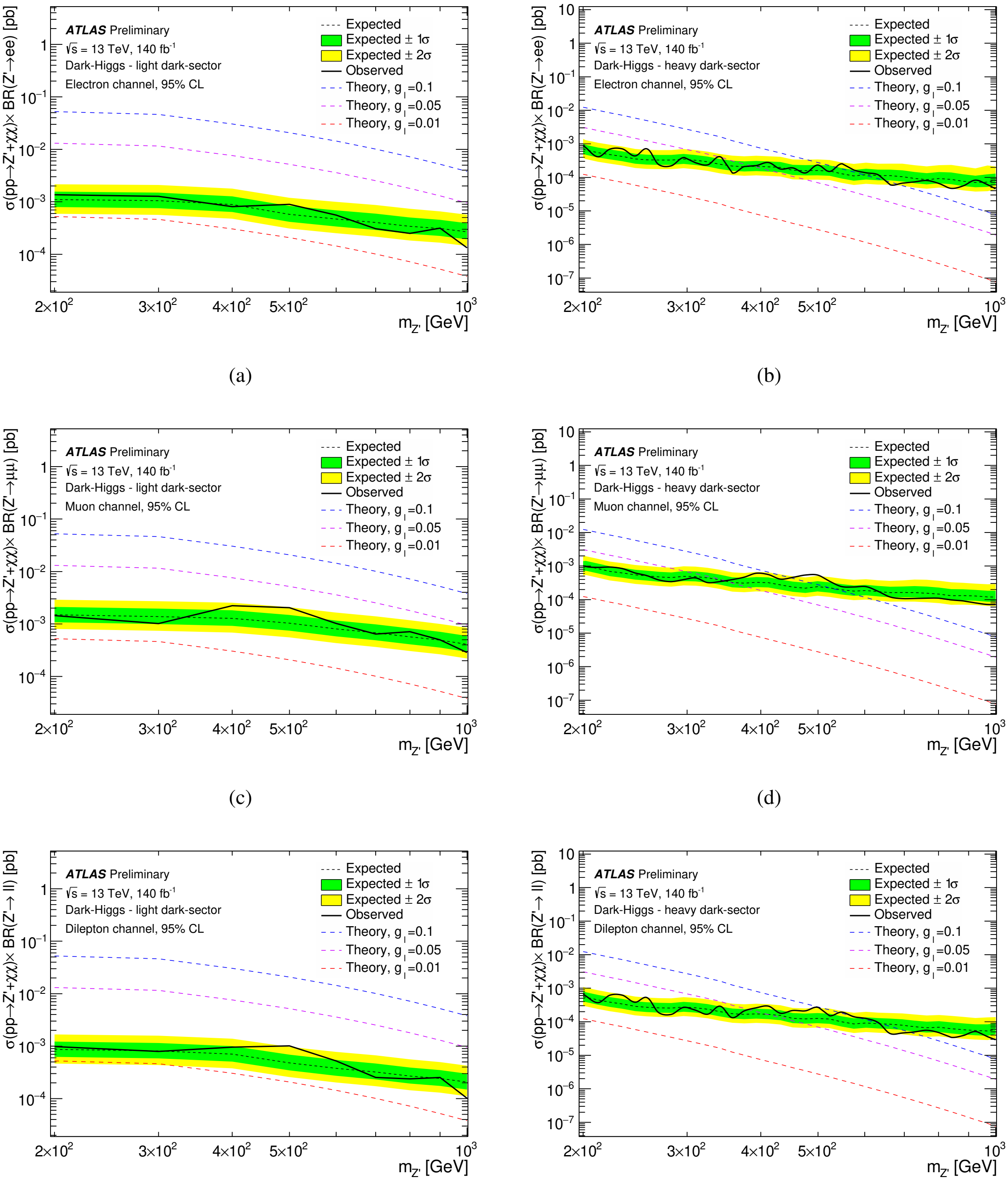

(a)

(b)

(c)

(d)

(e)

(f)

Figure 12: Observed and expected cross section limits for the dark-Higgs model with light dark-sector (left) and heavy dark-sector (right), shown for the electron channel (top), muon channel (middle) and the combined dilepton channel (bottom). The limits are obtained by combining the three SRs. The theory curves for $g_\ell = 0.05$ and $g_\ell = 0.1$ are obtained by assuming that the cross section scales as g_ℓ^2.

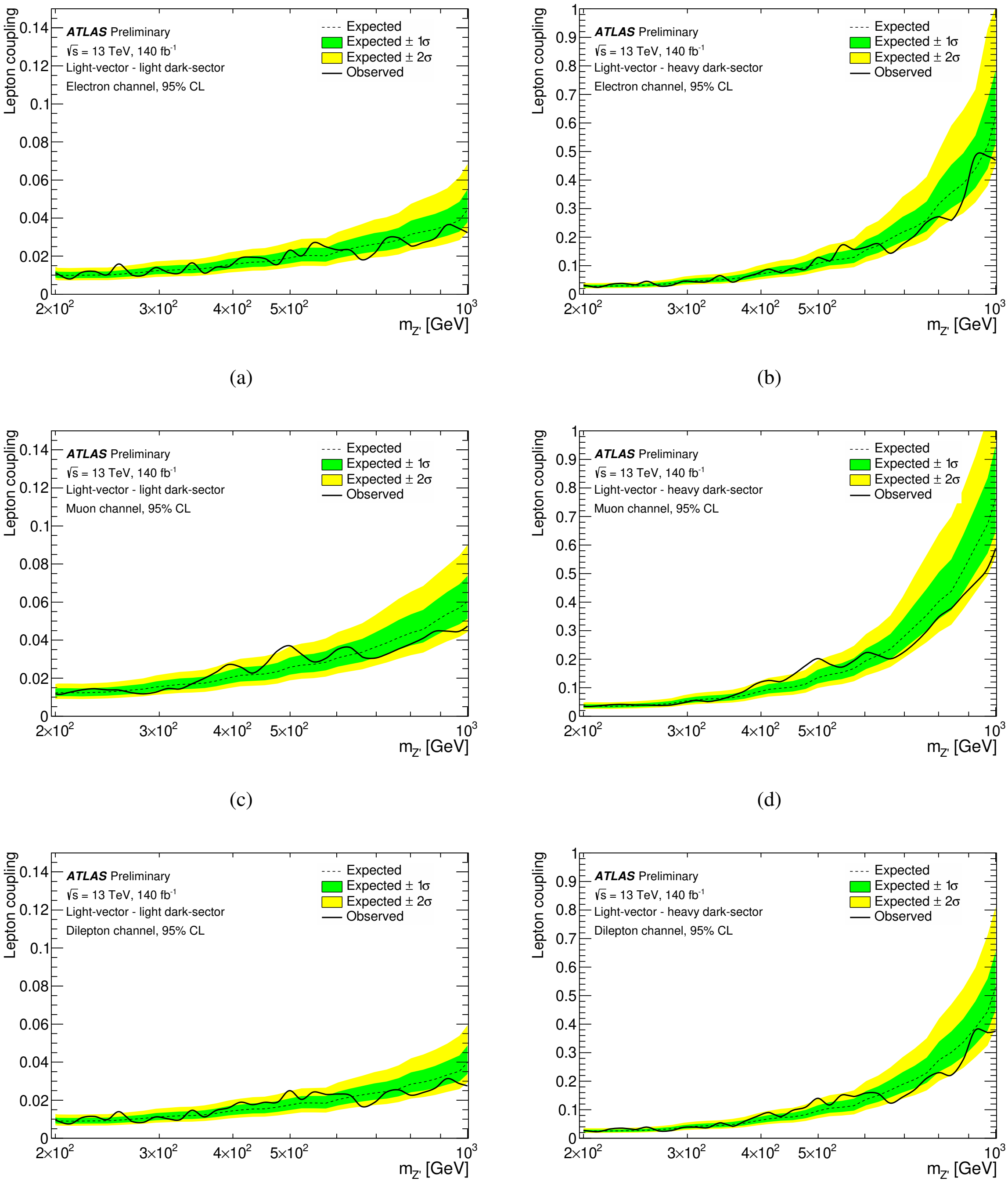

(a) (b)

(c) (d)

(e) (f)

Figure 13: Observed and expected lepton coupling limits for the light-vector model with light dark-sector (left) and heavy dark-sector (right), shown for the electron channel (top), muon channel (middle) and the combined dilepton channel (bottom). The limits are extracted from the cross section limit obtained by combining the three SRs.

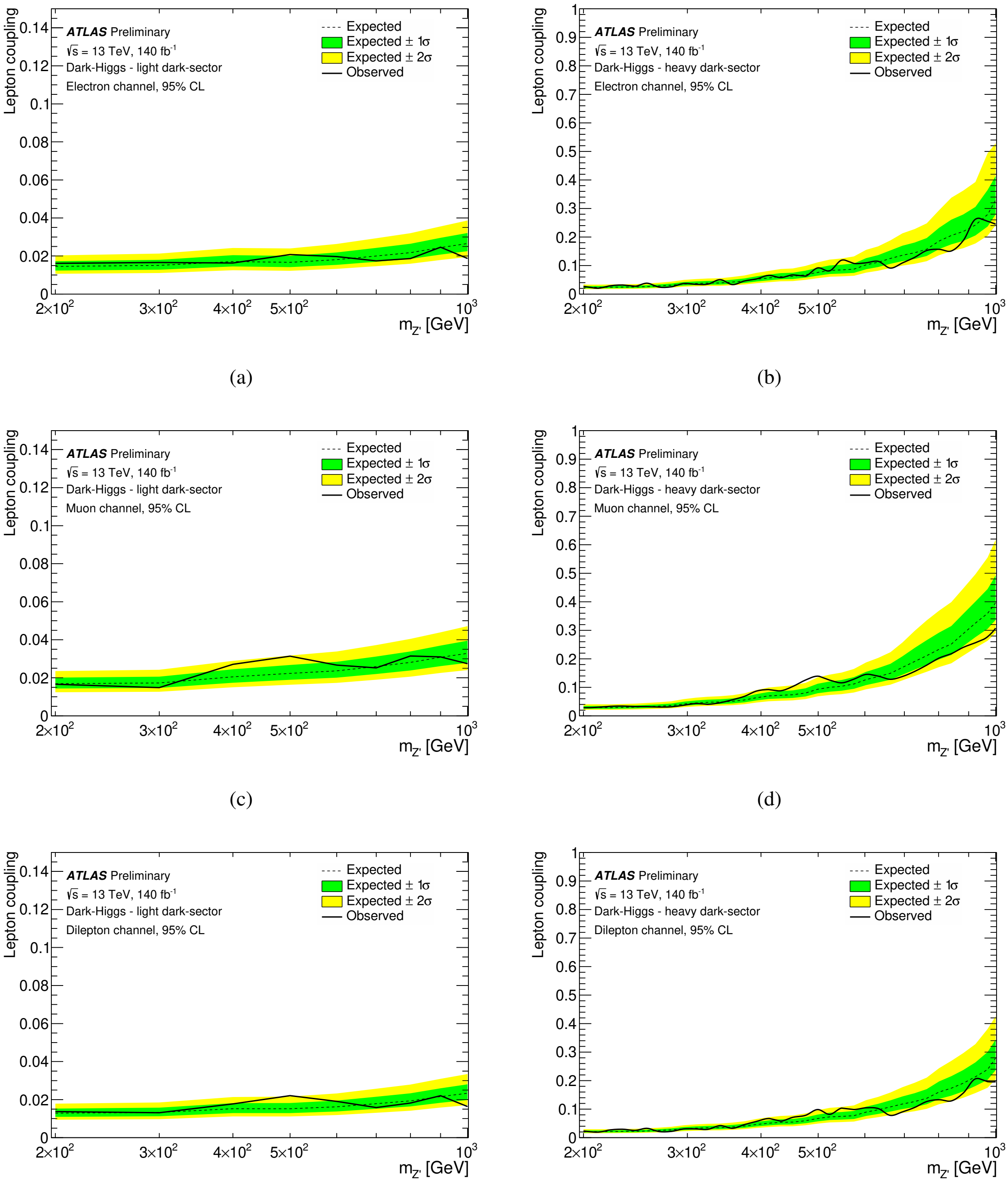

(a)

(b)

(c)

(d)

(e)

(f)

Figure 14: Observed and expected lepton coupling limits for the dark-Higgs model with light dark-sector (left) and heavy dark-sector (right), shown for the electron channel (top), muon channel (middle) and the combined dilepton channel (bottom). The limits are extracted from the cross section limit obtained by combining the three SRs.

Table 6: Exclusion limits on the cross section and the lepton coupling for $m_{Z'} = 500$ GeV, given for all four benchmark models in both the muon and electron channel.

Benchmark model	**Limit**	**Cross Section [pb]**		**Lepton Coupling**	
		ee	$\mu\mu$	ee	$\mu\mu$
Light Vector – light dark-sector	Expected	2.5×10^{-4}	4.6×10^{-4}	0.019	0.026
	Observed	3.6×10^{-4}	9.4×10^{-4}	0.023	0.037
Light Vector – heavy dark-sector	Expected	1.3×10^{-4}	2.1×10^{-4}	0.11	0.14
	Observed	1.9×10^{-4}	4.7×10^{-4}	0.13	0.20
Dark Higgs – light dark-sector	Expected	5.8×10^{-4}	1.0×10^{-3}	0.017	0.022
	Observed	8.9×10^{-4}	2.0×10^{-3}	0.021	0.031
Dark Higgs – heavy dark-sector	Expected	1.6×10^{-4}	2.4×10^{-4}	0.076	0.094
	Observed	2.3×10^{-4}	5.3×10^{-4}	0.091	0.14

9 Conclusion

A search for $e^{\pm}e^{\mp}$ and $\mu^{\pm}\mu^{\mp}$ resonances in final states with large missing transverse energy is presented. The search uses the complete dataset of proton-proton collisions at $\sqrt{s} = 13$ TeV recorded with the ATLAS detector during Run 2 of the LHC, corresponding to 140 fb^{-1}of integrated luminosity. No significant deviations from the SM are observed and the results are used to calculate limits as a function of the Z' mass as well as limits on the Z' coupling to leptons in the different benchmark models considered. Cross section exclusion limits are set for the light-vector model in the range of $1 \cdot 10^{-3}$ to $3 \cdot 10^{-5}$ pb and $4 \cdot 10^{-4}$ to $2 \cdot 10^{-5}$ pb for Z' masses between 200 and 1000 GeV in the light and heavy dark-sector scenarios, respectively. Corresponding limits of $1.5 \cdot 10^{-3}$ to $3 \cdot 10^{-4}$ pb and $5 \cdot 10^{-4}$ to $2 \cdot 10^{-5}$ pb for Z' masses between 200 and 1000 GeV are set in the light and heavy dark-sector for the dark-Higgs model, respectively. These limits assume $g_{\mathrm{D}} = 1$, $g_q = 0.1$, and $g_l = 0.01$ for both models. These benchmark signal models are presented as an example only, in particular because they have overabundant relic density [1, 4]. The resulting cross-section limits should be reinterpretable into other related models. For this purpose, separate limits are presented on the coupling of the Z' to the SM leptons, g_ℓ. These range from 0.01–0.025 and 0.02–0.38 for Z' masses between 200 and 1000 GeV for the light and heavy dark-sector in the light-vector model. For the dark-Higgs model the corresponding results are 0.014–0.02 and 0.02–0.2 for Z' masses between 200 and 1000 GeV in the light and heavy dark-sector scenarios, respectively. The limits obtained in this analysis significantly improve the limits on these models from a previous study performed using 11.6 fb^{-1}of CMS open-data collected during LHC Run 1 at a centre-of-mass energy of $\sqrt{s} = 8$ TeV [5], considering only the dimuon channel.

References

[1] M. Autran, K. Bauer, T. Lin, and D. Whiteson, *Searches for dark matter in events with a resonance and missing transverse energy*, Physical Review D **92** (2015), ISSN: 1550-2368, URL: `http://dx.doi.org/10.1103/PhysRevD.92.035007`.

[2] ATLAS Collaboration, *Search for high-mass dilepton resonances using 139 fb^{-1} of pp collision data collected at $\sqrt{s} = 13$ TeV with the ATLAS detector*, Phys. Lett. B **796** (2019) 68, arXiv: `1903.06248 [hep-ex]`.

[3] CMS Collaboration, *Search for resonant and nonresonant new phenomena in high-mass dilepton final states at $\sqrt{s} = 13$ TeV*, JHEP **07** (2021) 208, arXiv: `2103.02708 [hep-ex]`.

[4] ATLAS Collaboration, *Search for dark matter in events with a hadronically decaying vector boson and missing transverse momentum in pp collisions at $\sqrt{s} = 13$ TeV with the ATLAS detector*, JHEP **10** (2018) 180, arXiv: `1807.11471 [hep-ex]`.

[5] S. Elgammal, M. Louka, A. Y. Ellithi, and M. T. Hussein, *Search for the production of dark matter candidates in association with heavy dimuon resonance using the CMS open data for pp collisions at $\sqrt{s} = 8$ TeV*, (2021), arXiv: `2109.11274 [hep-ex]`.

[6] A. Albert et al., *Recommendations of the LHC Dark Matter Working Group: Comparing LHC searches for heavy mediators of dark matter production in visible and invisible decay channels*, (2017), URL: `https://arxiv.org/abs/1703.05703`.

[7] ATLAS Collaboration, *The ATLAS Experiment at the CERN Large Hadron Collider*, JINST **3** (2008) S08003.

[8] ATLAS Collaboration, *The ATLAS Collaboration Software and Firmware*, ATL-SOFT-PUB-2021-001, 2021, URL: `https://cds.cern.ch/record/2767187`.

[9] ATLAS Collaboration, *Performance of electron and photon triggers in ATLAS during LHC Run 2*, Eur. Phys. J. C **80** (2020) 47, arXiv: `1909.00761 [hep-ex]`.

[10] ATLAS Collaboration, *Performance of the ATLAS muon triggers in Run 2*, JINST **15** (2020) P09015, arXiv: `2004.13447 [hep-ex]`.

[11] ATLAS Collaboration, *ATLAS data quality operations and performance for 2015–2018 data-taking*, JINST **15** (2020) P04003, arXiv: `1911.04632 [physics.ins-det]`.

[12] ATLAS Collaboration, *Luminosity determination in pp collisions at $\sqrt{s} = 13$ TeV using the ATLAS detector at the LHC*, (2022), arXiv: `2212.09379 [hep-ex]`.

[13] G. Avoni et al., *The new LUCID-2 detector for luminosity measurement and monitoring in ATLAS*, JINST **13** (2018) P07017.

[14] ATLAS Collaboration, *The ATLAS Simulation Infrastructure*, Eur. Phys. J. C **70** (2010) 823, arXiv: `1005.4568 [physics.ins-det]`.

[15] GEANT4 Collaboration, S. Agostinelli, et al., *GEANT4 – a simulation toolkit*, Nucl. Instrum. Meth. A **506** (2003) 250.

[16] ATLAS Collaboration, *The simulation principle and performance of the ATLAS fast calorimeter simulation FastCaloSim*, ATL-PHYS-PUB-2010-013, 2010, URL: `https://cds.cern.ch/record/1300517`.

[17] T. Sjöstrand, S. Mrenna, and P. Skands, *A brief introduction to PYTHIA 8.1*, Comput. Phys. Commun. **178** (2008) 852, arXiv: `0710.3820 [hep-ph]`.

[18] R. D. Ball et al., *Parton distributions with LHC data*, Nucl. Phys. B **867** (2013) 244, arXiv: `1207.1303 [hep-ph]`.

[19] ATLAS Collaboration, *The Pythia 8 A3 tune description of ATLAS minimum bias and inelastic measurements incorporating the Donnachie–Landshoff diffractive model*, ATL-PHYS-PUB-2016-017, 2016, URL: `https://cds.cern.ch/record/2206965`.

[20] S. Frixione, G. Ridolfi, and P. Nason, *A positive-weight next-to-leading-order Monte Carlo for heavy flavour hadroproduction*, JHEP **09** (2007) 126, arXiv: `0707.3088 [hep-ph]`.

[21] P. Nason, *A new method for combining NLO QCD with shower Monte Carlo algorithms*, JHEP **11** (2004) 040, arXiv: `hep-ph/0409146`.

[22] S. Frixione, P. Nason, and C. Oleari, *Matching NLO QCD computations with parton shower simulations: the POWHEG method*, JHEP **11** (2007) 070, arXiv: `0709.2092 [hep-ph]`.

[23] S. Alioli, P. Nason, C. Oleari, and E. Re, *A general framework for implementing NLO calculations in shower Monte Carlo programs: the POWHEG BOX*, JHEP **06** (2010) 043, arXiv: `1002.2581 [hep-ph]`.

[24] T. Sjöstrand et al., *An introduction to PYTHIA 8.2*, Comput. Phys. Commun. **191** (2015) 159, arXiv: `1410.3012 [hep-ph]`.

[25] M. Beneke, P. Falgari, S. Klein, and C. Schwinn, *Hadronic top-quark pair production with NNLL threshold resummation*, Nucl. Phys. B **855** (2012) 695, arXiv: `1109.1536 [hep-ph]`.

[26] M. Cacciari, M. Czakon, M. Mangano, A. Mitov, and P. Nason, *Top-pair production at hadron colliders with next-to-next-to-leading logarithmic soft-gluon resummation*, Phys. Lett. B **710** (2012) 612, arXiv: `1111.5869 [hep-ph]`.

[27] P. Bärnreuther, M. Czakon, and A. Mitov, *Percent-Level-Precision Physics at the Tevatron: Next-to-Next-to-Leading Order QCD Corrections to* $q\bar{q} \to t\bar{t} + X$, Phys. Rev. Lett. **109** (2012) 132001, arXiv: `1204.5201 [hep-ph]`.

[28] M. Czakon and A. Mitov, *NNLO corrections to top-pair production at hadron colliders: the all-fermionic scattering channels*, JHEP **12** (2012) 054, arXiv: `1207.0236 [hep-ph]`.

[29] M. Czakon and A. Mitov, *NNLO corrections to top pair production at hadron colliders: the quark-gluon reaction*, JHEP **01** (2013) 080, arXiv: `1210.6832 [hep-ph]`.

[30] M. Czakon, P. Fiedler, and A. Mitov, *Total Top-Quark Pair-Production Cross Section at Hadron Colliders Through* $O(\alpha_S^4)$, Phys. Rev. Lett. **110** (2013) 252004, arXiv: `1303.6254 [hep-ph]`.

[31] M. Czakon and A. Mitov, *Top++: A program for the calculation of the top-pair cross-section at hadron colliders*, Comput. Phys. Commun. **185** (2014) 2930, arXiv: `1112.5675 [hep-ph]`.

[32] ATLAS Collaboration, *ATLAS Pythia 8 tunes to* 7 *TeV data*, ATL-PHYS-PUB-2014-021, 2014, URL: `https://cds.cern.ch/record/1966419`.

[33] R. D. Ball et al., *Parton distributions for the LHC run II*, JHEP **04** (2015) 040, arXiv: `1410.8849 [hep-ph]`.

[34] E. Re, *Single-top Wt-channel production matched with parton showers using the POWHEG method*, Eur. Phys. J. C **71** (2011) 1547, arXiv: `1009.2450 [hep-ph]`.

[35] N. Kidonakis, *Two-loop soft anomalous dimensions for single top quark associated production with a W^- or H^-*, Phys. Rev. D **82** (2010) 054018, arXiv: `1005.4451 [hep-ph]`.

[36] N. Kidonakis, “Top Quark Production”, *Proceedings, Helmholtz International Summer School on Physics of Heavy Quarks and Hadrons (HQ 2013)* (JINR, Dubna, Russia, July 15–28, 2013) 139, arXiv: `1311.0283 [hep-ph]`.

[37] E. Bothmann et al., *Event generation with Sherpa 2.2*, SciPost Phys. **7** (2019) 034, arXiv: `1905.09127 [hep-ph]`.

[38] T. Gleisberg and S. Höche, *Comix, a new matrix element generator*, JHEP **12** (2008) 039, arXiv: `0808.3674 [hep-ph]`.

[39] S. Schumann and F. Krauss, *A parton shower algorithm based on Catani–Seymour dipole factorisation*, JHEP **03** (2008) 038, arXiv: `0709.1027 [hep-ph]`.

[40] S. Höche, F. Krauss, M. Schönherr, and F. Siegert, *A critical appraisal of NLO+PS matching methods*, JHEP **09** (2012) 049, arXiv: `1111.1220 [hep-ph]`.

[41] S. Höche, F. Krauss, M. Schönherr, and F. Siegert, *QCD matrix elements + parton showers. The NLO case*, JHEP **04** (2013) 027, arXiv: `1207.5030 [hep-ph]`.

[42] S. Catani, F. Krauss, B. R. Webber, and R. Kuhn, *QCD Matrix Elements + Parton Showers*, JHEP **11** (2001) 063, arXiv: `hep-ph/0109231`.

[43] S. Höche, F. Krauss, S. Schumann, and F. Siegert, *QCD matrix elements and truncated showers*, JHEP **05** (2009) 053, arXiv: `0903.1219 [hep-ph]`.

[44] ATLAS Collaboration, *Multi-Boson Simulation for* 13 *TeV ATLAS Analyses*, ATL-PHYS-PUB-2017-005, 2017, URL: `https://cds.cern.ch/record/2261933`.

[45] C. Anastasiou, L. Dixon, K. Melnikov, and F. Petriello, *High-precision QCD at hadron colliders: Electroweak gauge boson rapidity distributions at next-to-next-to leading order*, Phys. Rev. D **69** (2004) 094008, arXiv: `hep-ph/0312266`.

[46] J. Alwall et al., *The automated computation of tree-level and next-to-leading order differential cross sections, and their matching to parton shower simulations*, JHEP **07** (2014) 079, arXiv: `1405.0301 [hep-ph]`.

[47] C. Bierlich et al., *A comprehensive guide to the physics and usage of PYTHIA 8.3*, 2022, arXiv: `2203.11601 [hep-ph]`.

[48] C. Anastasiou, L. Dixon, K. Melnikov, and F. Petriello, *High-precision QCD at hadron colliders: Electroweak gauge boson rapidity distributions at next-to-next-to leading order*, Phys. Rev. D **69** (9 2004) 094008, URL: `https://link.aps.org/doi/10.1103/PhysRevD.69.094008`.

[49] S. Dulat et al., *New parton distribution functions from a global analysis of quantum chromodynamics*, Phys. Rev. D **93** (2016) 033006, arXiv: `1506.07443 [hep-ph]`.

[50] S. G. Bondarenko and A. A. Sapronov, *NLO EW and QCD proton–proton cross section calculations with mcsanc-v1.01*, Computer Physics Communications **184** (2013) 2343, ISSN: 0010-4655, URL: `https://www.sciencedirect.com/science/article/pii/S0010465513001707`.

[51] ATLAS Collaboration, *Electron and photon performance measurements with the ATLAS detector using the 2015–2017 LHC proton–proton collision data*, JINST **14** (2019) P12006, arXiv: `1908.00005 [hep-ex]`.

[52] ATLAS Collaboration, *Muon reconstruction and identification efficiency in ATLAS using the full Run 2 pp collision data set at* $\sqrt{s} = 13$ *TeV*, Eur. Phys. J. C **81** (2021) 578, arXiv: `2012.00578 [hep-ex]`.

[53] ATLAS Collaboration, *Jet reconstruction and performance using particle flow with the ATLAS Detector*, Eur. Phys. J. C **77** (2017) 466, arXiv: `1703.10485 [hep-ex]`.

[54] M. Cacciari, G. P. Salam, and G. Soyez, *The anti-*k_t *jet clustering algorithm*, JHEP **04** (2008) 063, arXiv: `0802.1189 [hep-ph]`.

[55] ATLAS Collaboration, *Topological cell clustering in the ATLAS calorimeters and its performance in LHC Run 1*, Eur. Phys. J. C **77** (2017) 490, arXiv: `1603.02934 [hep-ex]`.

[56] ATLAS Collaboration, *Determination of jet calibration and energy resolution in proton–proton collisions at* $\sqrt{s} = 8$ *TeV using the ATLAS detector*, Eur. Phys. J. C **80** (2020) 1104, arXiv: `1910.04482 [hep-ex]`.

[57] ATLAS Collaboration, *Jet energy scale measurements and their systematic uncertainties in proton–proton collisions at* $\sqrt{s} = 13$ *TeV with the ATLAS detector*, Phys. Rev. D **96** (2017) 072002, arXiv: `1703.09665 [hep-ex]`.

[58] ATLAS Collaboration, *Selection of jets produced in* 13 *TeV proton–proton collisions with the ATLAS detector*, ATLAS-CONF-2015-029, 2015, URL: `https://cds.cern.ch/record/2037702`.

[59] ATLAS Collaboration, *Performance of pile-up mitigation techniques for jets in pp collisions at* $\sqrt{s} = 8$ *TeV using the ATLAS detector*, Eur. Phys. J. C **76** (2016) 581, arXiv: `1510.03823 [hep-ex]`.

[60] ATLAS Collaboration, *Forward jet vertex tagging using the particle flow algorithm*, ATL-PHYS-PUB-2019-026, 2019, URL: `https://cds.cern.ch/record/2683100`.

[61] *ATLAS flavour-tagging algorithms for the LHC Run 2 pp collision dataset*, (2022), arXiv: `2211.16345 [physics.data-an]`.

[62] ATLAS Collaboration,
Optimisation and performance studies of the ATLAS b-tagging algorithms for the 2017-18 LHC run,
ATL-PHYS-PUB-2017-013, 2017, URL: `https://cds.cern.ch/record/2273281`.

[63] M. Cacciari, G. P. Salam, and G. Soyez, *The Catchment Area of Jets*, JHEP **04** (2008) 005,
arXiv: `0802.1188 [hep-ph]`.

[64] ATLAS Collaboration,
E_T^{miss} *performance in the ATLAS detector using 2015–2016 LHC pp collisions*,
ATLAS-CONF-2018-023, 2018, URL: `https://cds.cern.ch/record/2625233`.

[65] ATLAS Collaboration,
Object-based missing transverse momentum significance in the ATLAS Detector,
ATLAS-CONF-2018-038, 2018, URL: `https://cds.cern.ch/record/2630948`.

[66] ATLAS Collaboration, *Vertex Reconstruction Performance of the ATLAS Detector at* $\sqrt{s} = 13$ *TeV*,
ATL-PHYS-PUB-2015-026, 2015, URL: `https://cds.cern.ch/record/2037717`.

[67] ATLAS Collaboration, *Estimation of non-prompt and fake lepton backgrounds in final states with top quarks produced in proton–proton collisions at* $\sqrt{s} = 8$ *TeV with the ATLAS Detector*,
ATLAS-CONF-2014-058, 2014, URL: `https://cds.cern.ch/record/1951336`.

[68] ATLAS Collaboration,
Search for new non-resonant phenomena in high-mass dilepton final states with the ATLAS detector,
JHEP **11** (2020) 005, arXiv: `2006.12946 [hep-ex]`, Erratum: JHEP **04** (2021) 142.

[69] ATLAS Collaboration, *Search for new phenomena in final states with two leptons and one or no b-tagged jets at* $\sqrt{s} = 13$ *TeV using the ATLAS detector*, Phys. Rev. Lett. **127** (2021) 141801,
arXiv: `2105.13847 [hep-ex]`.

[70] ATLAS Collaboration, *Electron reconstruction and identification in the ATLAS experiment using the 2015 and 2016 LHC proton–proton collision data at* $\sqrt{s} = 13$ *TeV*, Eur. Phys. J. C **79** (2019) 639,
arXiv: `1902.04655 [hep-ex]`.

[71] ATLAS Collaboration, *Jet energy scale and resolution measured in proton–proton collisions at* $\sqrt{s} = 13$ *TeV with the ATLAS detector*, Eur. Phys. J. C **81** (2020) 689,
arXiv: `2007.02645 [hep-ex]`.

[72] ATLAS Collaboration, *ATLAS b-jet identification performance and efficiency measurement with* $t\bar{t}$ *events in pp collisions at* $\sqrt{s} = 13$ *TeV*, Eur. Phys. J. C **79** (2019) 970,
arXiv: `1907.05120 [hep-ex]`.

[73] ATLAS Collaboration, *Measurement of the c-jet mistagging efficiency in* $t\bar{t}$ *events using pp collision data at* $\sqrt{s} = 13$ *TeV collected with the ATLAS detector*, Eur. Phys. J. C **82** (2021) 95,
arXiv: `2109.10627 [hep-ex]`.

[74] ATLAS Collaboration, *Calibration of light-flavour b-jet mistagging rates using ATLAS proton–proton collision data at* $\sqrt{s} = 13$ *TeV*, ATLAS-CONF-2018-006, 2018,
URL: `https://cds.cern.ch/record/2314418`.

[75] S. Schumann and F. Krauss,
A parton shower algorithm based on Catani-Seymour dipole factorisation,
Journal of High Energy Physics **2008** (2008) 038,
URL: `https://dx.doi.org/10.1088/1126-6708/2008/03/038`.

[76] S. Höche, S. Schumann, and F. Siegert,
Hard photon production and matrix-element parton-shower merging,
Phys. Rev. D **81** (3 2010) 034026,
URL: `https://link.aps.org/doi/10.1103/PhysRevD.81.034026`.

[77] T. P. S. Gillam and C. G. Lester, *Improving estimates of the number of 'fake' leptons and other mis-reconstructed objects in hadron collider events: BoB's your UNCLE*, JHEP **11** (2014) 031, arXiv: `1407.5624 [hep-ph]`.

[78] G. Cowan, K. Cranmer, E. Gross, and O. Vitells,
Asymptotic formulae for likelihood-based tests of new physics, Eur. Phys. J. C **71** (2011) 1554, arXiv: `1007.1727 [physics.data-an]`, Erratum: Eur. Phys. J. C **73** (2013) 2501.

[79] G. Altarelli, B. Mele, and M. Ruiz-Altaba, *Searching for new heavy vector bosons in $p\bar{p}$ colliders*, Z. Phys. C **45** (1989) 109, [Erratum: Z. Phys. C 47 (1990) 676].

[80] D. London and J. L. Rosner, *Extra gauge bosons in E(6)*, Phys. Rev. D **34** (1986) 1530.

[81] M. Baak, S. Gadatsch, R. Harrington, and W. Verkerke, *Interpolation between multi-dimensional histograms using a new non-linear moment morphing method*,
Nuclear Instruments and Methods in Physics Research Section A: Accelerators, Spectrometers, Detectors and Associated Equipment **771** (2015) 39, ISSN: 0168-9002,
URL: `https://www.sciencedirect.com/science/article/pii/S0168900214011814`.

[82] W. Verkerke and D. Kirkby, *The RooFit toolkit for data modeling*, 2003,
arXiv: `physics/0306116 [physics.data-an]`.

[83] L. Moneta et al., *The RooStats Project*, 2010, URL: `https://arxiv.org/abs/1009.1003`.

[84] K. Cranmer, G. Lewis, L. Moneta, A. Shibata, and W. Verkerke,
HistFactory: A tool for creating statistical models for use with RooFit and RooStats, tech. rep., New York U., 2012, URL: `https://cds.cern.ch/record/1456844`.

[85] A. L. Read, *Presentation of search results: the CL_S technique*, J. Phys. G **28** (2002) 2693.